buildings

MDPI

Article

Experimental Study and Finite Element Simulation of Externally Prestressed CFRP Plate Strengthened Pre-Cracked Reinforced Concrete T-Beam

Jiaqi Huang [1], Shunchao Chen [1,*], Peng Kang [2], Zhaohua Ma [1] and Ruipeng Wang [1]

1 School of Civil Engineering, Southwest Forestry University, Kunming 650224, China; huangjiaqi924@163.com (J.H.); 15287094554@163.com (Z.M.); 18469796258@163.com (R.W.)
2 Yunnan Institute of Building Research Co., Ltd., Kunming 650223, China; 19187109774@163.com
* Correspondence: csc99@163.com; Tel.: +86-187-2504-1841

Abstract

Cracking in reinforced concrete beam bridges severely compromises their durability and structural integrity. Although external prestressed CFRP plate reinforcement technology has emerged as an effective repair solution, current design codes primarily rely on idealized crack-free or simplified single-crack assumptions, leading to inadequate precision in prestressing application for real-world structures with complex crack networks. This study investigated the reinforcement effectiveness of externally prestressed CFRP plates on three pre-cracked reinforced concrete T-beams with varying reinforcement ratios (1.20%, 2.41%, and 3.61%). A comprehensive experimental program was conducted to monitor crack closure behavior, strain distributions, and deflection changes during tensioning and loading phases. A three-dimensional finite element model was developed using Midas FEA NX 2022, and theoretical formulas for crack closure prestressing were derived under the plane-section assumption, supplemented by engineering correction factors. Results demonstrated that calculation errors for both crack closure prestressing and secondary cracking loads were below 5%, while correlation coefficients between finite element simulations and experimental data ranged from 0.93 to 0.99. External prestressing significantly enhanced the stiffness of cracked beams, with stiffness recovery rates reaching up to 156.2%, and exhibited excellent synergistic performance among CFRP plates, steel reinforcement, and concrete. These findings provide a theoretical foundation and technical support for the precision design of external prestressing reinforcement in cracked reinforced concrete beams.

Keywords: reinforced concrete prestressed beam; external prestressing reinforcement; CFRP plate; stiffness repair; engineering correction factor; crack closure control; finite element simulation

Check for updates

Academic Editors: Zhongqiu Fu, Fangwen Wu and Qiudong Wang

Received: 24 April 2026
Revised: 14 May 2026
Accepted: 20 May 2026
Published: 22 May 2026

1. Introduction

The aging and deterioration of transportation infrastructure represents a pressing global challenge that intersects engineering, economic, and environmental sustainability concerns [1]. Reinforced concrete (RC) beam bridges, serving as critical arteries of highway networks worldwide, underpin the mobility of people and goods; yet their prolonged exposure to escalating traffic volumes, harsh climatic conditions, and deferred maintenance has precipitated a crisis of structural obsolescence [2–4]. In China alone, statistical surveys reveal that approximately 60% of over one million operational highway bridges exhibit crack-induced damage of varying severity [5]. These cracks initiate and propagate under the synergistic action of cyclic vehicular loads, environmental degradation—such as temperature and humidity fluctuations coupled with chloride ion ingress—and intrinsic material deterioration. Once formed, cracks precipitate a cascade of deleterious effects: local stiffness reduction, increased deflection, accelerated steel corrosion, and concrete carbonation, collectively eroding both safety margins and service lifespan. Against this backdrop, the development of efficacious reinforcement strategies and precision design methodologies for cracked RC beams transcends narrow disciplinary interest, constituting instead an engineering imperative with profound societal and economic ramifications.

Among the spectrum of available rehabilitation technologies, externally bonded prestressing reinforcement has gained prominence owing to its distinctive advantages: the active application of compressive stress, marked efficacy in closing existing cracks, and minimal increase in structural self-weight. Within this category, prestressed carbon fiber-reinforced polymer (CFRP) plates have emerged as the material of choice for modern prestressing systems. CFRP composites exhibit a remarkable combination of high tensile strength, elevated elastic modulus, and exceptional corrosion resistance—properties that address the limitations of conventional steel tendons. The underlying mechanism is conceptually elegant: by introducing a controlled reverse compressive stress state through externally bonded CFRP plates, the tensile stresses induced by service loads are counteracted, thereby promoting crack closure and restoring the structural stiffness that was compromised by prior damage [6].

Nevertheless, a fundamental bottleneck impedes the widespread engineering adoption of this promising technology. The prestressing calculation models codified in current design standards—exemplified by China's JTG/T 5431-2025 and GB50367-2013 [7,8]-rest predominantly upon idealized assumptions of either crack-free members or simplified single-crack geometries. Such idealizations demonstrate inadequate adaptability to the intricate crack networks encountered in actual structures, where multi-crack interactions and three-dimensional crack morphologies govern mechanical behavior. Compounding this theoretical limitation, engineering practice frequently relies on empirical prestressing values, yielding suboptimal precision: excessive prestressing risks concrete crushing or premature CFRP rupture [9], whereas insufficient prestressing fails to achieve complete crack closure, leaving the intended reinforcement effect unrealized. These deficiencies have catalyzed an active scholarly debate. One school of thought contends that classical smeared-crack models, rooted in continuum damage mechanics, suffice for engineering design despite their abstraction of discrete fracture features. An opposing perspective argues that such simplifications incur unacceptable predictive errors when applied to complex crack networks, advocating instead for fracture-mechanics-based approaches that explicitly resolve individual crack geometry and interaction. The tension between computational tractability and physical fidelity remains unresolved, underscoring the urgent need for prestressing calculation methodologies that are rigorously grounded in actual crack characteristics-an essential prerequisite for attaining "precision reinforcement" in deteriorated RC beams.

A substantial body of literature, developed across several decades and multiple continents, has endeavored to elucidate the relationship between crack characteristics and prestressed reinforcement effectiveness. International research commenced earlier and has followed two discernible methodological trajectories. The first trajectory, rooted in fracture mechanics, traces to Lutz [10], who in the 1980s established foundational theoretical principles for crack analysis and experimentally demonstrated the influence of crack width on prestress transfer efficiency. Building upon this foundation, Jalali et al. [11] proposed a quantitative relationship between crack closure degree and applied prestress magnitude; however, their formulation was strictly limited to idealized single through-cracks, leaving its validity for multi-crack scenarios untested. Panagiotakos and Li [12,13] subsequently advanced the field by incorporating crack spacing effects and refining the prestress calculation framework, though their model likewise neglected the coupled influence of three-dimensional crack morphology and environmental degradation factors. A second, more recent trajectory has embraced computational approaches-finite element and mesh-free methods-to capture crack network complexity, yet these studies often sacrifice the closed-form simplicity required for routine engineering design.

Since the 1990s, relevant domestic research has developed rapidly. Focusing on empirical parametric analysis, the theoretical system of crack information parameters has been established. Crack width, length and direction are systematically integrated to form unified evaluation indicators for reinforcement effect. In the following decades, calculation models of reinforcement effect were derived based on the plane section assumption and strain compatibility principle [14–16]; while mathematically tractable, these models have demonstrated limited predictive fidelity when confronted with the irregular crack patterns characteristic of field conditions. These parallel research streams have converged upon an unsettled question: whether reinforcement design should prioritize theoretical rigor—resolving individual crack mechanics at computational expense—or pragmatic parameterization that captures dominant behavioral trends through simplified indicators. This epistemic tension, between explanatory depth and engineering utility, directly motivates the present investigation.

In recent years, increasing attention has been devoted to the rehabilitation of damaged reinforced concrete members using prestressed FRP systems under complex service environments. Recent studies have demonstrated that the interaction among prestress level, crack morphology, confinement effects, and pre-existing damage conditions significantly influences stiffness recovery, crack closure efficiency, and long-term structural performance. Particularly, damage-dependent prestress transfer mechanisms and confinement-enhanced crack control behavior have become important research topics for deteriorated RC members subjected to realistic loading conditions.

Recent investigations have also highlighted that the mechanical behavior of prestressed FRP-strengthened members cannot be fully characterized solely through idealized single-crack assumptions. Instead, multi-crack interactions, nonlinear damage accumulation, and environmental coupling effects may substantially affect reinforcement efficiency and structural reliability. Specifically, Shayanfar et al. [17] demonstrated that prestress efficiency in heat-damaged RC columns is significantly influenced by the coupling among pre-existing damage states, prestress levels, and confinement mechanisms, providing a quantitative framework for damage-dependent prestress evaluation. Ranjbar et al. [18] further elucidated the seismic response and damage mechanisms of RC systems considering soil–structure interaction, highlighting the necessity of incorporating realistic boundary and loading conditions in reinforcement design. These recent advances collectively underscore the need for prestress evaluation methodologies that explicitly account for crack characteristics, non-ideal effects, and complex service environments—a gap that the present study addresses through an integrated experimental–theoretical–numerical framework. These findings further emphasize the necessity of developing prestress design approaches that explicitly incorporate crack characteristics and engineering non-idealities. Therefore, the present study attempts to bridge the gap between theoretical simplicity and engineering realism through an integrated experimental–theoretical–numerical framework capable of evaluating crack-closure prestress in pre-cracked reinforced concrete T-beams strengthened with externally prestressed CFRP plates.

A critical synthesis of the foregoing literature reveals three conspicuous deficiencies that circumscribe current understanding. First, prevailing closed-form models exhibit limited adaptability to the multi-crack, three-dimensional fracture systems ubiquitous in actual engineering structures; they fail to adequately capture the nonlinear influence of crack network topology on prestress transfer pathways [19]. Second, existing formulations lack systematic quantification of non-ideal engineering factors—including prestress loss due to anchorage slip and long-term relaxation, anchorage system efficiency, and material property discreteness—creating persistent discrepancies between theoretical predictions and field performance. Third, the parametric coupling between structural design variables (notably longitudinal reinforcement ratio) and the magnitude of crack-closure prestress remains insufficiently elucidated, impeding the development of versatile design guidelines adaptable to diverse member configurations.

To redress these gaps, the present study investigates the flexural strengthening of precracked RC T-beams using externally bonded prestressed CFRP plates, pursuing an integrated experimental–analytical–computational methodology. The primary research objectives are threefold: (1) to design and execute strengthening experiments on three full-scale T-beams with varying reinforcement ratios, systematically acquiring mechanical response data-including strain distributions, deflection profiles, crack-closure prestress levels, and secondary cracking loads throughout tensioning and subsequent loading phases-thereby illuminating the influence of reinforcement ratio on crack-closure behavior and stiffness recovery; (2) to derive a closed-form in situ prestress calculation formula grounded in the plane-section assumption, deformation compatibility principles, and moment equilibrium theory, supplemented by empirically calibrated correction factors that account for non-ideal effects, together with recommended coefficient ranges for typical design scenarios; and (3) to construct and validate a three-dimensional finite element model in Midas FEA NX 2022 that incorporates nonlinear material constitutive laws and explicit crack morphology, verifying both the analytical formula and the numerical model through multi-dimensional comparisons against experimental measurements. The central conclusion establishes that crack-closure prestress can be predicted with engineering accuracy by combining classical sectional analysis with crack-characteristic-dependent correction factors, thereby bridging the gap between fracture-mechanics fidelity and design-office practicality. These findings furnish a rigorous theoretical foundation and actionable technical guidance for the precision design of external prestressing reinforcement in deteriorated RC beams, advancing the methodology from empirical art toward quantifiable engineering science.

2. Materials and Methods

2.1. Experimental Program

This experimental investigation utilized three simply supported T-section reinforced concrete beams, designated as A1, A2, and A3, each with a span of 6.8 m. The specimens possessed a total length of 7000 mm and a height of 540 mm, fabricated with C40-grade concrete. The web cross-section measured 170 mm × 540 mm, with an effective flange width of 600 mm × 100 mm and a clear cover thickness of 30 mm. Reinforcement configurations are detailed in Table 1. A water-cement ratio of 0.38 was adopted for the concrete, with the corresponding mix proportions provided in Table 2. The beams were fabricated in compliance with the JTG 3362-2018 [20] specification using full-height steel formwork and vibration compaction techniques, followed by 28 days of natural curing to allow for material aging prior to load testing. Following this curing period, fatigue loading was applied to induce permanent cracking within the mid-span pure bending region. The precracked specimens exhibited at least three vertical cracks with stabilized widths extending beyond half the beam height, thereby satisfying the preliminary crack criteria essential for external prestressing reinforcement testing. The constituent materials adopted in the concrete mix proportion are as follows. P·O 42.5 ordinary Portland cement was supplied by Yiliang Hongshi Cement Co., Ltd. (Yiliang, China). All aggregates were provided by Yunnan Construction Investment Sand and Stone Materials Co., Ltd. (Kunming, China). Reinforcing bars were supplied by Yunnan Qujing Chenggang Iron and Steel (Group) Co., Ltd. (Qujing, China). The CFRP plates for reinforcement were supplied by Nanjing Mankate Technology Co., Ltd. (Nanjing, China).

Table 1. Test parameters of flexural members.

Sample Number	Sample Size				Longitudinal Tendon		Stirrup	
	b/mm	h/mm	b′f/mm	h′f/mm	Longitudinal Tendon	Ratio of Reinforcement	Longitudinal Tendon	Ratio of Reinforcement
A1	160	540	600	100	2-Φ25	1.20%	Φ8@60	1.05%
A2	160	540	600	100	4-Φ25	2.41%	Φ8@60	1.05%
A3	160	540	600	100	6-Φ25	3.61%	Φ8@60	1.05%

Table 2. Concrete mix ratio and design strength.

Cement	Water	Stone Silt Sand	Sand Dust	Fine Crushed Stone	Medium-Sized Crushed Aggregate	Design Strength Grade for Concrete	Water-Cement Ratio
450	225	440	160	400	800	C40	0.38

The experimental program was systematically organized into four sequential phases: (1) initial graded loading to induce controlled cracking in the pure bending region; (2) incremental tensioning of the CFRP plate until complete crack closure; (3) post-strengthening graded loading until secondary crack stabilization; and (4) post-release graded loading after prestress removal. Each phase involved three loading cycles with comprehensive data acquisition of load, strain, deflection, and crack parameters.

The beam dimensions and reinforcement are shown in Figures 1 and 2. The bottom tension longitudinal bars of the web are: A1 = 2-Φ25, A2 = 4-Φ25, and A3 = 6-Φ25. The vertical bars for the flange plate are all 8-Φ12, while those for the web are all 2-Φ8. Web stirrups: within the 2 m span center, Φ8@120; elsewhere, Φ8@60; flange plate stirrups throughout the span are Φ8@60. The core materials used in the tests were C40 concrete, HRB400 grade reinforcement bars, and CFRP plates for reinforcement. Standard test results confirmed that their mechanical properties fully met design and code requirements; the material mechanical parameters are presented in Table 3.

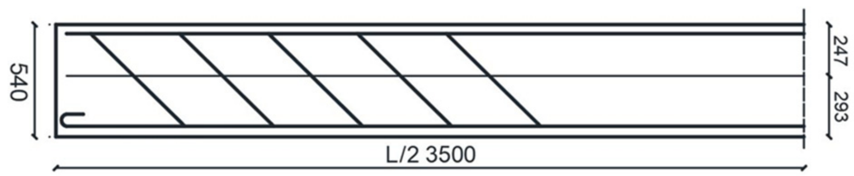

Figure 1. Longitudinal dimensions of T-beam L/2.

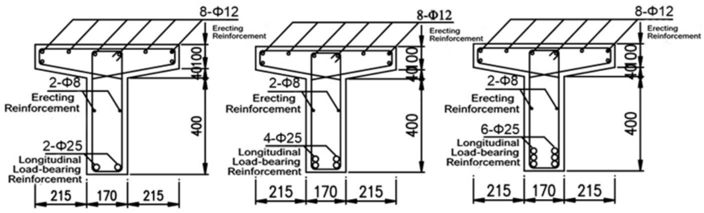

Figure 2. Cross-section dimensions of T-beams.

Table 3. Mechanical properties of materials/MPa.

Material Type (Including Specifications)		Core Mechanical Performance Indicators	Numeric Value	Remarks
C40 concrete		Cubic compressive strength (mean value)	49.2 (mean, SD = 2.25)	The measured average values for the samples in Group 2
		Prism compressive strength (mean value)	38.7 (mean, SD = 1.83)	The measured average values for all three test specimens
HRB400 grade steel reinforcement	Φ8	yield strength	400	GB 50010-2010 Specification Value
		ultimate tensile strength	/	
	Φ12	yield strength	400	
		ultimate tensile strength	/	
	Φ25 (main reinforcement)	yield strength	460	Actual measured values of the main reinforcement bars and the bent-up reinforcement bars
		ultimate tensile strength	590	
Reinforcement using CFRP plates (single-layer 50 mm × 2 mm, double-layered stack)		Axial tensile strength	≥2800	GB50367-2013 specification value
		modulus of elasticity	$\geq 1.6 \times 10^5$	
		interlaminar shear strength	≥50	
		Fracture elongation rate	≥1.6%	

Note: SD–Standard Deviation; both tensile and compressive strength values are measured values or representative values according to specifications.

2.2. Test Device and Loading Protocol

The CFRP plates were subjected to three-point loading using an MTS electro-hydraulic servo fatigue testing machine (MTS Systems Corporation, Eden Prairie, MN, USA), with graded tension applied via a calibrated hydraulic jack (5 kN per stage; testing conducted after each stage reached stable load). Detailed loading conditions are shown in Table 4. The measurement system consisted of a DH3819 wireless static strain acquisition system (Jiangsu Donghua Testing Technology Co., Ltd., Jingjiang, China), dial gauges (Harbin Measuring & Cutting Tool Co., Ltd., China General Technology Group, Harbin, China) (at mid-span and support points), and a crack width tester (Beijing Newlead Technology Co., Ltd., Beijing, China). The CFRP plate was anchored using clip-type anchorage devices and high-strength chemical bolts, with reinforcement structures installed at the anchorage ends.

The loading protocol employed an MTS electro-hydraulic servo fatigue testing machine under load-controlled mode for all phases. The control and loading system of MTS fatigue testing machine is shown in Figure 3. Each load increment was maintained for 2–3 min to allow stabilization before data recording. Loading was terminated when reaching 80% of the estimated ultimate load or when mid-span deflection exceeded L/250. The

CFRP tensioning was performed using a calibrated hydraulic jack with wedge grips and anchor plates, with three repeated tensioning cycles to minimize anchorage slip effects.

Table 4. Loading Condition (s).

Loading Phase	Control Mode	Increment (kN)	Loading Rate (kN/min)	Hold Time (min)	Cycles	Max Load/Force (kN)
Phase 1: Initial loading (pre-cracking)	Load	5	5	2	3	110
Phase 2: CFRP tensioning	Force	10	2	3	3	110.6/81.4/73.2
Phase 3: Post-strengthening loading	Load	5	5	2	3	50/58/60
Phase 4: Post-release loading	Load	5	5	2	3	50/58/60

(a)

(b)

Figure 3. Electric hydraulic servo structure fatigue testing machine. (**a**) MTS fatigue testing machine control system. (**b**) MTS fatigue testing machine loading system.

In the experimental system, displacement transducers were installed at the mid-span and support locations, while strain gauges were arranged at the upper concrete surface, lower concrete surface, reinforcement bars, and CFRP plates. The loading was applied through a hydraulic actuator under graded loading control. Simply supported boundary conditions were adopted. The left end used a pinned support (steel hinge assembly), constraining translational degrees of freedom in X, Y and Z directions (UX = UY = UZ = 0) while allowing rotation about the X-axis (ROTX free). The right end used a roller support, constraining vertical and transverse translations (UY = UZ = 0) while allowing longitudinal movement (UX free) and rotation about the X-axis (ROTX free). Rotations about Y and Z axes were restrained at both ends (ROTY = ROTZ = 0). The schematic diagram of T-beam loading and measuring point layout is shown in Figures 4 and 5.

The experiment was conducted uniformly in four phases, with simultaneous collection of load, strain, deflection, and crack data throughout the entire process.

- Pre-cracking preparation: Apply graded loads to the pure bending section at the beam mid-span to generate at least three vertical cracks with stable widths extending half the beam height; record the initial crack parameters and mechanical reference values.
- Pre-stressing tensioning: Gradually tension the CFRP plate until all cracks have closed, then anchor it to complete the reinforcement.
- Post-reinforcement loading: Apply graded loads again until secondary cracking stabilizes, then record the secondary cracking load, stiffness, and crack propagation.

- Post-unloading loading: After releasing the tensile force, perform three re-classified loadings and record the residual deformation and ultimate stress characteristics.

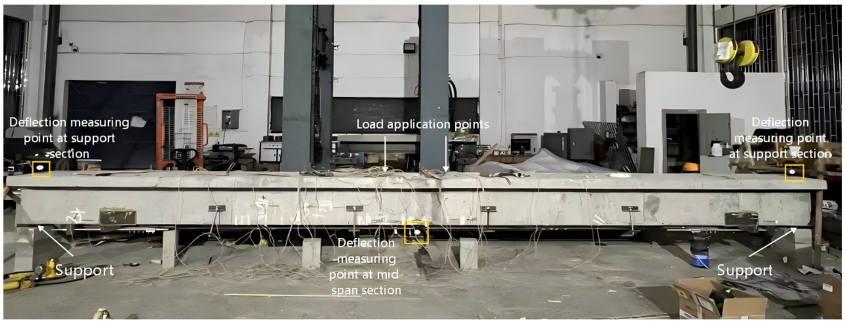

Figure 4. Schematic Layout of T-beam Loading and Deflection Measuring Points.

Figure 5. Loading Schematic of T-Beam.

The termination criteria for each loading phase were as follows: Phase 1 was terminated when at least three vertical cracks with stabilized widths exceeding half the beam height were formed; Phase 2 was terminated when all visible cracks were completely closed and the target tension force was reached; Phase 3 was terminated upon stabilization of secondary cracking; and Phase 4 was terminated when significant residual deformation was observed or load capacity degraded by more than 15% from the peak value.

2.3. Finite Element Modeling

2.3.1. Establishment of the Geometric Model

Using the Midas FEA NX 2022 software [21], based on the geometric parameters and loading conditions of the test beam, the model consists of a main beam, a reinforcement system (including main reinforcement, stirrups, web reinforcement, and tie bars), a CFRP plate (including the anchorage and tension ends), and supports/loading pads. The CFRP plate was geometrically modeled according to the parameters specified in the Highway Bridge Reinforcement Design Code (JTG/T522-2019) [22]. The reinforcement was integrated into a skeletal structure through a one-dimensional element array translation, with the entire structure formed via Boolean operations. The final integrated model is shown in Figure 6.

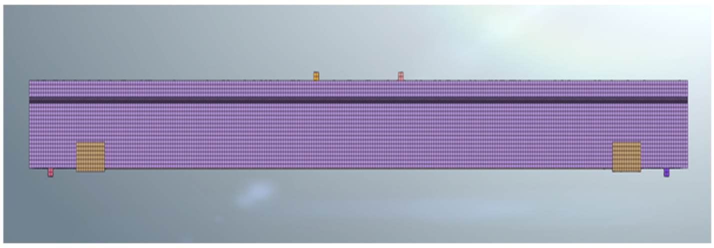

Figure 6. Geometric Model Establishment.

The FE model was developed using MIDAS FEA NX 2022 software. Concrete was modeled using SOLID65 eight-node hexahedral elements with a mesh size of 50 mm. Reinforcement was simulated using LINK180 two-node bar elements. The CFRP plate was modeled using SOLID185 eight-node hexahedral elements. Nonlinear analysis adopted displacement-controlled loading with a convergence tolerance of 0.5% and a maximum of 150 iterations per step.

In the finite element model, one support end was constrained in the vertical and longitudinal directions, while the other support end was constrained only in the vertical direction to avoid over-constraint effects. Coupling constraints were introduced between the CFRP anchorage zone and the concrete beam to simulate prestress transfer behavior.

2.3.2. Material Constitutive Relationship

The nonlinear analysis of C40 concrete employs the plastic damage model for concrete [23–25], accounting for asymmetric tensile-compressive behavior to describe the damage evolution during tensile cracking and compressive fracture. The elastic modulus is 3.25 × 104 MPa, the Poisson's ratio is 0.2, and the compressive strengths of cubes and prisms are 49.2 MPa and 38.7 MPa, respectively (experimental averages). The tensile-compressive constitutive laws and damage parameters are determined in accordance with the Code for Design of Concrete Structures (GB 50010-2010) [26]. Elastic analysis utilizes the linear elastic constitutive model with parameters identical to those for nonlinear analysis; the uniaxial tensile stress–strain relationship is calculated using Equations (1)–(4), while the uniaxial compressive relationship is calculated using Equations (5)–(9).

$$\sigma = (1 - d_t) E_c \varepsilon \tag{1}$$

$$d_t = \begin{cases} 1 - \rho_t \left[1.2 - 0.2x^5\right], & x, 1 \\ 1 - \frac{\rho_t}{\alpha_t (x-1)^{1.7} + x}, & x > 1 \end{cases} \tag{2}$$

$$x = \frac{\varepsilon}{\varepsilon_{t,r}} \tag{3}$$

$$\rho_t = \frac{f_{t,r}}{E_c \varepsilon_{t,r}} \tag{4}$$

where α_t = parameter value of the descending segment of the concrete uniaxial tensile curve; $f_{t,r}$ = uniaxial tensile strength of concrete; $\varepsilon_{t,r}$ = peak tensile strain of concrete corresponding to $f_{t,r}$; E_c = elastic modulus of concrete; d_t = uniaxial tensile damage evolution parameter of concrete.

$$\sigma = (1 - d_c) E_c \varepsilon \tag{5}$$

$$d_c = \begin{cases} 1 - \frac{\rho_c n}{n-1+x^n} & x, 1 \\ 1 - \frac{\rho_c}{\alpha_c (x-1)^2 + x} & x > 1 \end{cases} \tag{6}$$

$$\rho_c = \frac{f_{c,r}}{E_c \varepsilon_{c,r}} \tag{7}$$

$$n = \frac{E_c \varepsilon_{c,r}}{E_c \varepsilon_{c,r} - f_{c,r}} \tag{8}$$

$$x = \frac{\varepsilon}{\varepsilon_{c,r}} \tag{9}$$

where α_t = parameter of the descending branch of the uniaxial compression curve of concrete; $f_{c,r}$ = uniaxial compressive strength of concrete; $\varepsilon_{c,r}$ = peak compressive strain of concrete corresponding to $f_{c,r}$; E_c = modulus of elasticity of concrete; d_c = damage evolution parameter of concrete under uniaxial compression.

The HRB400 grade reinforcement employs a double-folded-line elastic–plastic constitutive model (including a yield plateau), with an elastic modulus of 210 GPa and a Poisson's ratio of 0.3. For the Φ25 main reinforcement, the yield strength is 460 MPa and the ultimate strength is 590 MPa, based on experimental measurements; for other specifications (Φ8, Φ12), the values refer to those specified in the code. The slope of the hardening segment is calculated using the code formula. According to GB50010-2010, the reinforcement's yield strength, ultimate strength, and stress–strain relationship can be determined.

$$\begin{aligned} f_{ym} &= f_{yk} / (1 - 1.645\delta_s) \\ f_{stm} &= f_{stk} / (1 - 1.645\delta_s) \end{aligned} \tag{10}$$

where f_{ym} = mean yield strength of steel reinforcement; f_{stm} = mean ultimate strength of steel reinforcement; f_{yk} = characteristic yield strength of steel reinforcement; f_{stk} = characteristic ultimate strength of steel reinforcement; δ_s = coefficient of variation in steel strength.

$$\sigma_s = \begin{cases} E_s \varepsilon_s & \varepsilon_s \le \varepsilon_y \\ f_{y,r} & \varepsilon_y < \varepsilon_s \le \varepsilon_{uy} \\ f_{y,r} + k(\varepsilon_s - \varepsilon_{uy}) & \varepsilon_{uy} < \varepsilon_s \le \varepsilon_u \\ 0 & \varepsilon_s > \varepsilon_u \end{cases} \tag{11}$$

$$\varepsilon_y = \frac{f_{y,r}}{E_s} \tag{12}$$

$$k = \frac{f_{st,r} - f_{y,r}}{\varepsilon_u - \varepsilon_{uy}} \tag{13}$$

where σ_s = steel stress; ε_s = steel strain; E_s = modulus of elasticity of steel reinforcement; $f_{y,r}$ = representative yield strength of steel; in this paper, the standard yield strength of steel f_{yk} is adopted; $f_{st,r}$ = representative ultimate strength of steel; in this paper, the standard ultimate strength of steel reinforcement f_{stk} is adopted; ε_u = ultimate strain of steel corresponding to $f_{st,r}$; ε_{uy} = strain at the onset of steel strain hardening; ε_y = yield strain of steel corresponding to $f_{y,r}$; k = slope of the steel strain-hardening segment.

The CFRP plate is a high-strength linearly elastic material with no distinct yield stage, employing an ideal linear elastic constitutive model. Its parameters are derived from the "Code for Design of Highway and Bridge Reinforcement" (JTG/T 522-2019) and actual product measurements: tensile strength $\geq$ 2800 MPa, elastic modulus $\geq 1.6 \times 105$ MPa, shear strength $\geq$ 50 MPa, fracture elongation $\geq$ 1.6%, and Poisson's ratio 0.3. The CFRP plate exhibits linear elasticity without plastic deformation prior to failure, consistent with experimental characteristics. The relationship between the carbon fiber's elastic stage and its fracture behavior is illustrated in Equations (14) and (15).

$$\sigma_{cf} = E_{cf}\varepsilon_{cf} \quad 0 \leq \varepsilon_{cf} \leq \varepsilon_{cfu} \tag{14}$$

$$\sigma_{cf} = 0, E_{cf} = 0 \quad \varepsilon_{cf} > \varepsilon_{cfu} \tag{15}$$

where σ_{cf} = stress of CFRP plate, f_{cfu} = ultimate tensile strength of carbon CFRP plate, E_{cf} = modulus of elasticity of CFRP plate, ε_{cfu} = ultimate tensile strain of CFRP plate.

2.3.3. Grid Division and Simulation Methods

After defining the material properties for each cross-section, assign the corresponding section parameters to the respective structural members. Concrete and CFRP plates are discretized using hexahedral solid elements (grid size: 25 mm), while the reinforcement system is simulated with embedded beam elements (element length: 100 mm). The grid division results are shown in Figure 7.

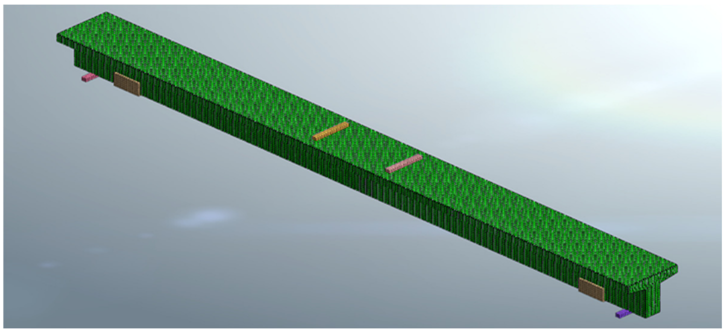

Figure 7. Grid division of experimental beams.

The number of units in regions A1–A3 is 76,052,77,432, and 78,812, respectively, corresponding to node counts of 77,543,78,572, and 79,607. Coupling constraints are established between the anchoring/tensioning end nodes and the CFRP plate nodes, achieving displacement coordination with the bottom nodes of the concrete beam through longitudinal and transverse degree-of-freedom coupling. The numerical calculations employ both linear and nonlinear solvers; the nonlinear analysis sets an upper limit of 150 incremental steps, activates geometric nonlinear effects, and utilizes a displacement convergence criterion along with a linear search algorithm to ensure computational stability.

2.3.4. Simulation Analysis of Concrete Beam Cracks

The crack model was constructed using the entity-based element elimination technique [27,28]: first, geometric parameters were obtained using a crack width tester (see Figure 8), followed by the removal of corresponding elements from the model. The equivalent width simulation method was employed to simplify the actual crack into five typical cracks (see Figure 9).

In Figure 9, the corresponding crack location is highlighted within the yellow box, with crack widths labeled as C1–C5.

A hierarchical loading model was established using Midas FEA NX 2022; after incorporating the crack model, the numerical analysis results improved significantly, validating the effectiveness of the crack treatment method. This approach has since been adopted for all subsequent concrete crack analyses.

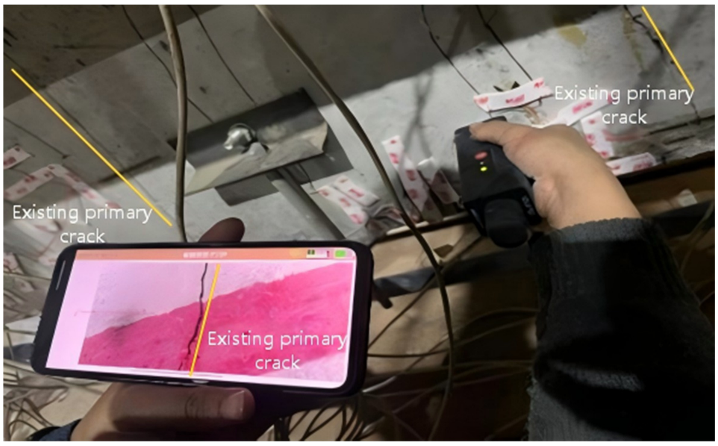

Figure 8. Record of crack parameters in T-beams.

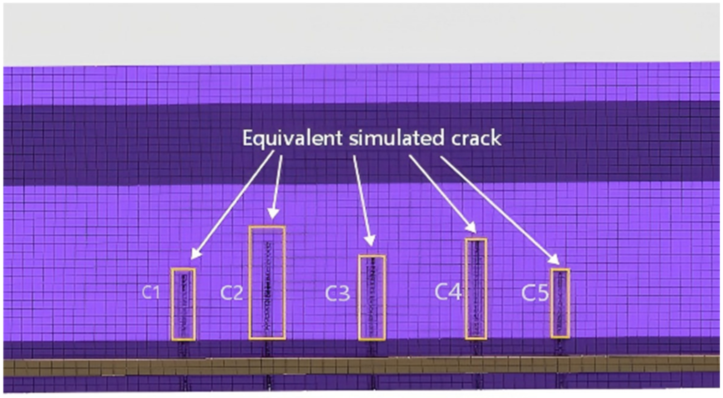

Figure 9. Simulation of mid-span cracks in T-beams.

It should be noted that the present crack simulation approach is based on predefined crack morphology and equivalent-width element deletion. This method can effectively reproduce the stiffness reduction and stress redistribution induced by existing cracks, and is therefore suitable for engineering-oriented prestress evaluation. However, the approach does not explicitly simulate progressive crack propagation, fracture energy evolution, or adaptive crack path development during loading. Consequently, the model is more appropriate for macroscopic structural response analysis rather than detailed fracture-mechanics investigation.

2.4. Theoretical Framework

During the tensioning process of prestressed CFRP plates, under the assumption of a flat cross-section, cracks gradually close under the applied tensile force until a crack-free state is achieved. In the initial stage, the tensile force is converted into pressure on the reinforcement through stress transfer, with the main reinforcement bearing the concrete pressure. When the cracks are fully closed, the main reinforcement is completely compressed, and the tensile force equals the pressure on the reinforcement, achieving mechanical equilibrium and ensuring structural stability.

Although reinforced concrete beams may exhibit nonlinear strain distributions after cracking, experimental measurements in the present study indicated that the strain profiles across the beam depth remained approximately linear before secondary cracking, particularly after the externally applied prestress promoted crack closure and stiffness recovery. Therefore, within the investigated loading range, the plane-section assumption remains reasonably applicable for engineering prestress evaluation.

In the early stage of crack closure, the constitutive relationship governing steel bar compression can be derived from the deformation coordination condition [29–32]:

$$\varepsilon_S = \frac{w}{L} \tag{16}$$

In the formula $wL\varepsilon_S$ represents the total width of the crack, denotes the longitudinal length range of the crack along the beam, and indicates the strain of the reinforcement.

Based on the generalized Hooke's law, a stress–strain $\sigma_s \varepsilon_s E_s$ relationship is established, showing a linear correlation between the stress and strain of steel reinforcement and the elastic modulus, expressed as:

$$\sigma_s = E_s \varepsilon_s \tag{17}$$

Substituting the previously derived formula (16) into the above equation yields:

$$\sigma_s = E_s \frac{w}{L} \tag{18}$$

The equivalent pressure F on the steel reinforcement is:

$$F = \sigma_S A \tag{19}$$

where σ_s = compressive stress acting on the steel reinforcement; A = cross-sectional area of the reinforcement.

The cross-sectional area A_s of the steel reinforcement can be calculated based on the number of reinforcing bars n and the diameter d of a single bar. For round reinforcing bars, the total cross-sectional area A_s of n bars is:

$$A_s = \frac{n\pi d^2}{4} \tag{20}$$

Given the compressive stress σ_s acting on the steel reinforcement and its cross-sectional area A_s, the compressive force F applied to the reinforcement can be obtained according to Equation (19):

$$F = \sigma_s A_s = E_s \times \frac{w}{L} \times \frac{n\pi d^2}{4} \tag{21}$$

The calculation of the section moment of inertia of a T-beam is complicated. The section is usually divided into simple geometric shapes, such as rectangles or trapezoids, and then calculated in combination using the parallel axis theorem. First, the moment of inertia I_o of each part about its own centroidal axis is calculated; for example, rectangular sections have a specific formula.

$$I_o = \frac{bh^3}{12} \tag{22}$$

For the upper flange:

$$I_{f0} = \frac{b_f h_f^3}{12} \tag{23}$$

For the web plate:

$$I_{w0} = \frac{b_w h_w^3}{12} \tag{24}$$

For the lower flange:

$$I_{l0} = \frac{b_l h_l^3}{12} \tag{25}$$

Then, according to the parallel translation axis formula:

$$I_l = I_0 + Ad^2 \tag{26}$$

where I_l = the moment of inertia of the section relative to the desired axis; I_0 = the moment of inertia of the section relative to its own centroidal axis; A = the cross-sectional area; d = the perpendicular distance between the desired axis and the centroidal axis.

The moment of inertia of each part is transformed to the neutral axis of the T-beam, where A_i is the cross-sectional area of each part, and d_i is the distance from the centroidal axis of each part to the neutral axis of the T-beam. Assume that the distance from the neutral axis of the T-beam to the top surface of the upper flange is y_1, to the top surface of the web is y_2, and to the bottom surface of the lower flange is y_3.

The moment of inertia I_f of the upper flange about the neutral axis of the T-beam is:

$$I_f = I_{f0} + b_f h_f \left(y_1 - \frac{h_f}{2} \right)^2 \tag{27}$$

The moment of inertia I_1 of the lower flange about the neutral axis of the T-beam is:

$$I_1 = I_{10} + b_f h_{f1}(h - y_3) - \frac{h_{f1}^2}{2} \tag{28}$$

The total moment of inertia I of the T-beam is the sum of the moments of inertia of each component:

$$I = I_f + I_w + I_n \tag{29}$$

where I = total moment of inertia of the T-beam; I_1 = moment of inertia of each component about the neutral axis of the T-beam; b_f = width of the top flange of the T-beam; h_f = thickness of the top flange of the T-beam; b_w = width of the web of the T-beam; h_w = height of the web of the T-beam; b_{f1} = width of the bottom flange of the T-beam; h_{f1} = thickness of the bottom flange of the T-beam; H = total height of the T-beam; y_1 = distance from the neutral axis of the T-beam to the top surface of the top flange; y_2 = distance from the neutral axis of the T-beam to the bottom surface of the bottom flange; y_3 = distance from the neutral axis of the T-beam to the bottom surface of the web; A = cross-sectional area of each component (top flange, web, bottom flange); d = distance from the centroid of each component to the neutral axis of the T-beam.

Based on the moment equilibrium principle, the torque equation relating the steel bar compression force to the CFRP plate tension force on the neutral axis is established to determine the required CFRP plate tension force for complete crack closure. When the crack closes, the two torque forces are equal, i.e.,

$$F \times y_s = N \times y_c \tag{30}$$

Substituting Equation (30) derived earlier into the above equation, the tensile force N of the CFRP plate can be obtained as:

$$N = \frac{F \times y_s}{y_c} = \frac{E_s w n \pi d^2 y_s}{4 L y_c} \tag{31}$$

where N = tensile force of the CFRP plate, F = compressive force acting on the steel reinforcement, y_s = distance from the main reinforcement to the neutral axis, y_c = distance from the CFRP plate to the neutral axis.

Bending moment equilibrium is a fundamental principle in structural mechanics for analyzing reinforced concrete compression members, reflecting a structure's capacity to withstand stable deformation. By calculating the moments of steel reinforcement and CFRP plates, overall stability is ensured. From an energy perspective, bending moment equilibrium implies energy conservation in the direction of rotation, with external work and internal strain energy being in equilibrium, thereby guaranteeing structural performance.

After the CFRP plate is tensioned, the beam exhibits camber. As the load increases, the camber decreases, and the reinforcement in the tension zone changes from compression to tension. When the bending moment M_{ex} is less than M_0 (the decompression moment), no tensile stress develops in the beam; when M_{ex} equals M_0, the beam is in a stress-free state. With further loading, secondary cracking occurs in the beam, which verifies the accuracy of the prestress calculation.

At this stage, the structure is subjected to an eccentric prestressing force N and a vertical load P, which is calculated using the eccentric compression formula. The most unfavorable section of the simply supported beam is near the support points, with the compressive stress at the bottom edge of the mid-span taken as the control index.

When only prestress is applied, the normal stress in the fibers at the bottom edge of the beam is:

$$\sigma_{cl} = \frac{N}{A_0} + \frac{N \cdot e_0 \cdot y_0}{I_0} \tag{32}$$

where N = effective prestressing force of the tendons, A_n = transformed cross-sectional area, I_n = moment of inertia of the transformed section about the neutral axis, e_n = eccentricity of the prestressing force relative to the transformed section, y_0 = distance from the bottom fiber of the beam to the neutral axis of the transformed section.

The external bending moment exerted by the transverse load on the beam:

$$M_{ex} = \frac{\sigma_{ck} \cdot I_n}{y_0} \tag{33}$$

where $e_t{}'$ = distance from the bottom fiber of the beam to the neutral axis of the transformed section.

Thus, M_{pe}, the equivalent counter-bending moment generated by the effective prestress, is equal to the external bending moment M_{ex} applied to the beam by the mid-span load.

$$M_{ex} = M_{pe} \tag{34}$$

where M_{pe} is the equivalent counter-bending moment generated by the effective prestress.

The mid-span P load value is:

$$M = P \cdot x_1 \tag{35}$$

where x_1 = horizontal distance (moment arm) from the load application point to the support.

The mid-span cracking P_1 load value is:

$$P_1 = \frac{N - T_c}{N/P} \tag{36}$$

where N = prestress value of the CFRP plate after anchorage (kN), T_c = prestress for continued tensioning to close cracks (kN).

3. Results

3.1. Stress Performance Analysis Before Reinforcement

The three concrete beams were subjected to graded loading: the maximum test loads for A1 were 80 kN, for A2 were 129.93 kN, and for A3 were 130.01 kN. The core mechanical properties of the specimens during the loading phase prior to reinforcement are shown in Table 5, while the load–deflection relationship is illustrated in Figure 10.

Table 5. Core Mechanical Properties of Specimens during Preloading Stage after Strengthening.

Sample Number	Ultimate Load (kN)	Stiffness Under a 30 kN Load (N/mm)	Mid-Span Deflection Under Ultimate Load (mm)	Initial Crack Characteristics
A1	80.00	7.08	−12.47	3 vertical cracks, with a width of 0.2–0.3 mm
A2	129.93	8.41	−15.22	3 vertical cracks, with a width of 0.15–0.25 mm
A3	130.01	9.09	−13.08	3 vertical cracks, with a width of 0.1–0.2 mm

Note: A negative deflection value indicates upward arching, while a positive value indicates downward deflection; stiffness is calculated based on the mid-span deflection.

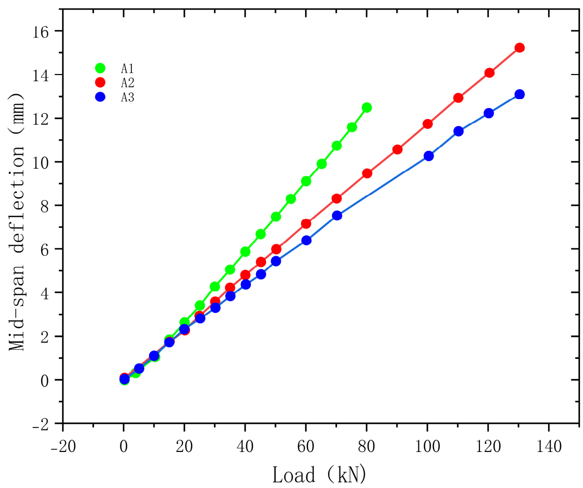

Figure 10. Relationship Diagram between the Mid-span Deflection and the Load Level.

The fitting analysis using Origin 2024 software revealed that the stress behavior of all three beams exhibited the typical sequence of "elastic stage-cracking stage-yield stage," with stiffness values ranked as A3 > A2 > A1, confirming the reinforcing effect of increased main reinforcement on beam flexural stiffness. For instance, under a 30 kN load, the stiffness values of A1, A2, and A3 were 7.08 N/mm, 8.41 N/mm, and 9.09 N/mm, respectively; the higher reinforcement ratio significantly enhanced deformation resistance through improved section confinement.

It is noted that the ultimate load of specimen A1 (80 kN) is significantly lower than those of A2 (129.93 kN) and A3 (130.01 kN). This difference is mainly attributed to the variation in longitudinal reinforcement ratios, which are 1.20%, 2.41%, and 3.61% for A1, A2, and A3, respectively. A higher reinforcement ratio enhances the flexural capacity and initial stiffness of the beams, resulting in higher ultimate loads for A2 and A3.

However, it should also be noted that the number of specimens in this study is limited, and the influence of test variability cannot be completely excluded. Therefore, the observed difference reflects both the genuine effect of reinforcement ratio and possible specimen-to-specimen variation. Future studies with a larger number of specimens will be conducted to further verify this conclusion.

3.2. Analysis of the Prestressing Tensioning Stage

3.2.1. Strain Analysis of Measured Concrete, Reinforcement, and CFRP Plates

Using a calibrated hydraulic jack to apply graded tension to the CFRP plates, the maximum tension forces for A1, A2, and A3 were 100.60 kN, 81.40 kN, and 73.20 kN, respectively. The comprehensive strain results of the specimens during the tensioning stage are presented in Table 6, while the tension–force–strain relationship is shown in Figure 11.

The fitting results indicate that the tensile force exhibits a piecewise linear relationship with strain, with a distinct inflection point during crack closure corresponding to closure forces of A1: 35.70 kN, A2: 23.10 kN, and A3: 34.60 kN. Prior to closure, the strain growth rate at A1 was significantly higher than at A2 and A3; the confinement effect of the main reinforcement resulted in a more gradual strain increase in the highly reinforced beam. At the instant of closure, the strain jump was maximum at A1 (+15%) and minimum at A2 (+8%), demonstrating the regulatory influence of the number of main reinforcement bars on transient mechanical behavior. Post-closure, the difference in strain distribution was less than 5%, indicating a significant improvement in collaborative efficiency.

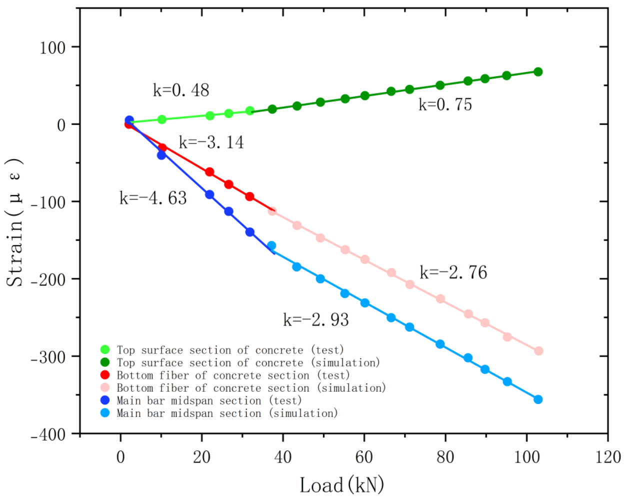

(**a**) A1 Strain-Load Relationship Diagram

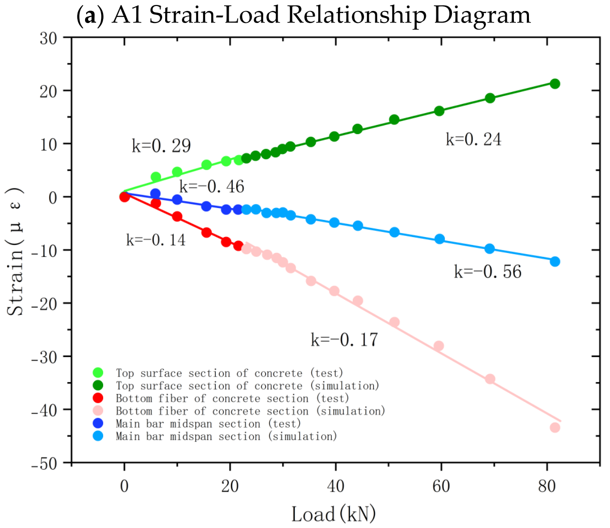

(**b**) A2 Strain-Load Relationship Diagram

Figure 11. *Cont.*

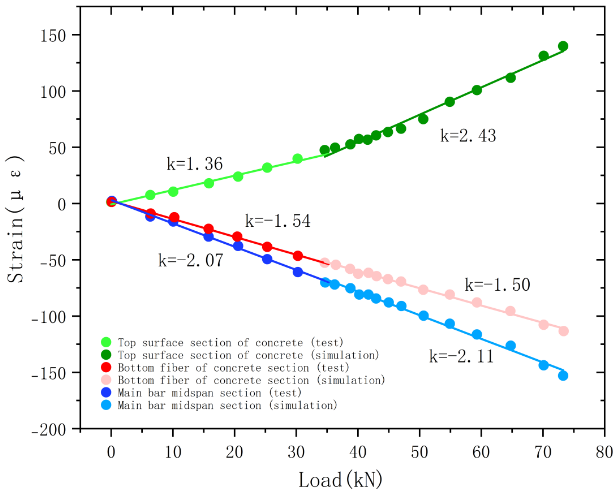

(**c**) A3 Strain-Load Relationship Diagram

Figure 11. Relationship Diagram between the Measured Strain and the Load Level.

Table 6. Comprehensive strain results of specimens during tensioning phase (under critical tension force, unit: με).

Tension Node	Test-Piece	Strain at the Upper Edge of the Concrete/με	Strain at the Bottom Edge of the Concrete/με	Main Reinforcement Strain/με	CFRP Plate L/2 Strain/με
Critical value for fracture closure	A1	16.95	−93.90	−139.45	1012.39
	A2	7.32	−9.77	−2.44	825.70
	A3	46.70	−53.10	−69.58	2641.93
Maximum tensile force	A1	67.17	−293.20	−356.05	3296.59
	A2	21.30	−43.33	−12.21	2675.17
	A3	139.49	−113.52	−152.87	5484.18

Note: Tensile strain is positive, while compressive strain is negative; the average value of measurement points is taken for each cross-section.

3.2.2. Analysis of Actual Concrete Deflection Results

This study presents a measured analysis of concrete deflection in beam prestressing reinforcement tests. CFRP plates were tensioned in stages, with maximum tensile forces reaching 100.6 kN, 81.40 kN, and 73.20 kN. The relationship between specimen deflection during tensioning and crack closure prestress is shown in Table 7, while the correlation between measured deflection and load levels is illustrated in Figure 12.

Table 7. Deflection and Crack Closure Prestress of Specimens During Tensioning Stage.

Sample Number	Critical Prestress for Crack Closure (kN)	Mid-Span Deflection Under Critical Prestress (mm)	Maximum Tensile Force (kN)	Mid-Span Deflection Under Maximum Tensile Force (mm)	Deflection Increase Slope (mm/kN) Before/After Closure
A1	35.70	−2.01	100.60	−4.48	−0.06/−0.04
A2	23.10	−0.43	81.40	−2.41	−0.02/−0.04
A3	34.60	−1.02	73.20	−2.50	−0.03/−0.04

Note: A negative deflection value indicates upward curvature; the slope represents the linear fit from the Origin.

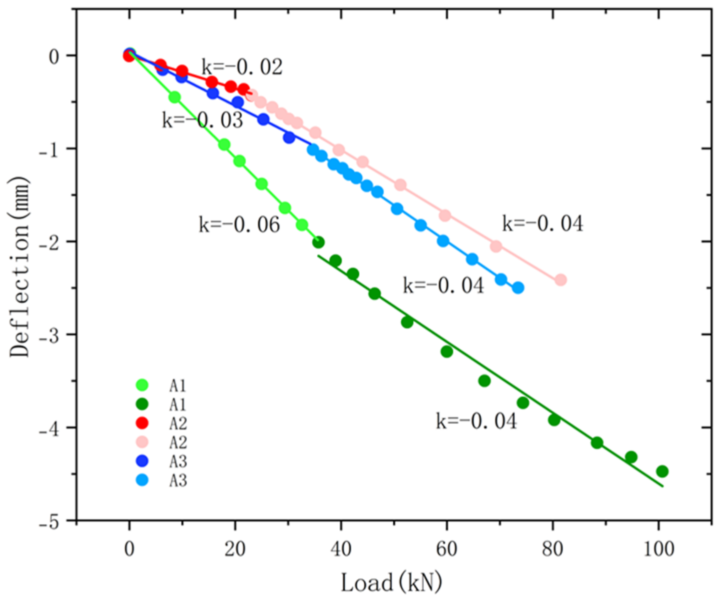

Figure 12. Relationship Diagram between the Measured Deflection and the Load Level.

The fitting results show that before crack closure, the deflection growth slopes of A1, A2, and A3 were −0.06, −0.02, and −0.03 mm/kN, respectively, while after closure, they all decreased to −0.04 mm/kN, indicating significant stiffness recovery. Under the same tensile force, the deflection order was A1 > A2 > A3, with A3 demonstrating the highest deformation resistance due to its optimal reinforcement ratio.

3.3. Analysis of Stress Performance After Reinforcement

After completing the tensioning and anchoring of the CFRP plate, the concrete beam underwent graded loading. The core mechanical properties of the specimen during the post-reinforcement loading stage are presented in Table 8, while the measured tension force–strain data are plotted in Figure 13.

Table 8. Core Mechanical Properties of Specimens during Post-Strengthening Loading Stage.

Sample Number	Secondary Cracking Load (kN)	Stiffness Under a 30 kN Load (N/mm)	Mid-Span Deflection Under a 50 kN Load (mm)	Strain of CFRP Plate Under a 50 kN Load (με)	Stiffness Recovery Rate (%)
A1	15.00	11.89	5.47	548.80	156.2
A2	18.00	9.81	5.16	198.58	117.3
A3	11.91	9.02	5.33	249.58	104.5

Note: Stiffness recovery rate = Post-reinforcement stiffness/Pre-reinforcement stiffness × 100%.

The fitting results indicate that the secondary cracking loads after reinforcement follow a non-monotonic distribution (A1: 15.00 kN, A2: 18 kN, A3: 11.91 kN). The load–deflection relationship prior to cracking exhibits a strong linear correlation ($R^2 \geq 0.98$), with A1 showing the smallest deflection under the same load. Post-cracking stiffness degradation for A1 (64%) exceeds that of A3 (5%), demonstrating the delay effect of prestressing on crack propagation and the stiffness loss characteristics following crack expansion.

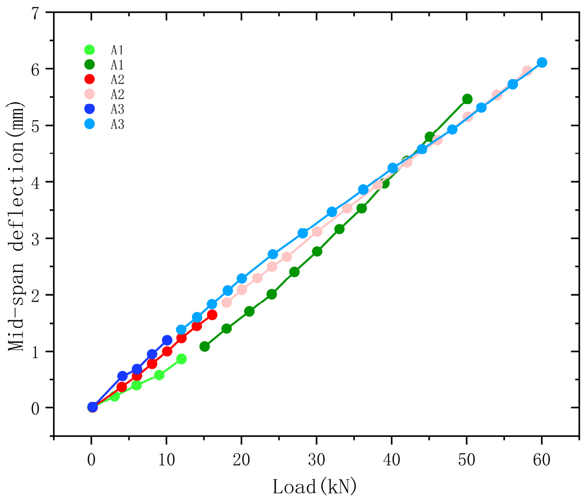

Figure 13. Relationship Diagram between the Measured Deflection and the Load Level.

3.4. Analysis of the T-Beam Loading Test Results After Unloading of CFRP Plates

After unloading the CFRP plates, loading tests were conducted on A2 and A3. The obtained tensile force–deflection data are plotted as shown in Figure 14.

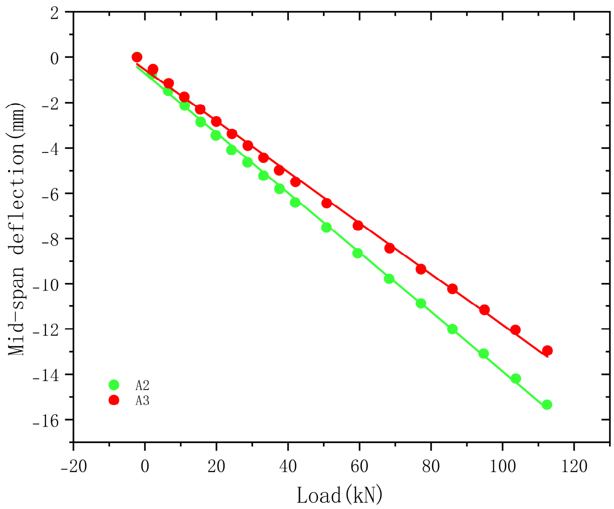

Figure 14. Relationship Diagram between the Measured Deflection and the Load Level.

The fitting results indicate that both A2 and A3 exhibit ultimate loads of approximately 130 kN, with their load–deflection curves exhibiting a gradual transition from linear to nonlinear behavior without distinct cracking or yield inflection points. The initial stiffness of A3 (9.33 kN/mm) is significantly higher than that of A2 (6.52 kN/mm), and the deflection at ultimate load for A3 (12.95 mm) is 15.4% lower than that of A2, confirming the constraining effect of the high reinforcement ratio on deformation.

3.5. Finite Element Simulation Results

This study employed the Midas FEA NX 2022 software to conduct comparative elastic and nonlinear analyses of prestressed CFRP plate-reinforced concrete beams. The prestressing forces on the CFRP plates were set as A1 = 100.00 kN, A2 = 80.00 kN, and A3 = 75.00 kN; after reinforcement, the loading forces on the T-beam were A1 = 50.00 kN, A2 = 58.00 kN, and A3 = 60.00 kN. The comparisons between experimental results during the prestressing stage and finite element simulations, as well as between post-reinforcement loading conditions, are presented below. Numerical simulation data on strain of the concrete, steel reinforcement, and CFRP plate, along with mid-span deflection measurements of the beam, demonstrate that under prestressing forces of 37.55 kN, 25.12 kN, and 35.86 kN respectively, all cracks in specimens A1, A2, and A3 closed. Beam stiffness progressively recovered and continuously increased with rising prestressing levels. The application of prestress introduced a reverse compressive stress field that effectively counteracted tensile stresses at crack locations, facilitating crack closure. Secondary cracking occurred in cracks A1, A2, and A3 at loads of 13.76 kN, 14.31 kN, and 11.91 kN, respectively. As loads increased, accumulated tensile stresses exceeded residual compressive stresses and the concrete's tensile strength thresholds, leading to crack re-opening (secondary cracking).

Figure 15 illustrates the stress distribution and transfer during the elastic stage of a prestressed CFRP plate-reinforced concrete pre-cracked beam, validating the reliability of the Midas FEA NX model. The stress gradient at the mid-span exhibits significant variation, with the maximum tensile stress at the L/2 section of the CFRP plate reaching 551.24 MPa, consistent with material properties; the concrete compression zone demonstrates uniform stress distribution, featuring a minimum compressive stress of −11.89 MPa, indicating that the prestress induces counteracting compressive stress to counteract the external tensile stress, aligning with the crack closure mechanism. The stress transfer efficiency is high, with stress contributions ranging from 4.4% to 34.3% across all regions, reflecting the synergistic interaction among the CFRP plate, reinforcement, and concrete. Prestress is transmitted efficiently without stress concentration or interruption, confirming the effectiveness of the meshing and crack simulation methods. The results conform to the plane section assumption, validating the appropriateness of the material constitutive parameters and providing a basis for subsequent analyses and engineering applications. The simulation focuses solely on the elastic stage and does not account for nonlinear crack propagation effects; future work may incorporate crack propagation criteria to enhance accuracy.

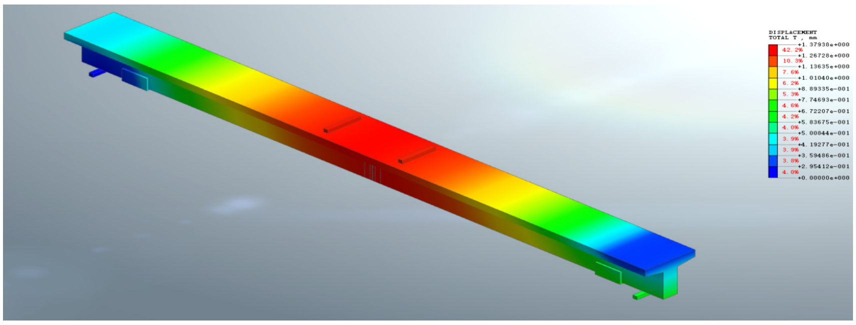

Figure 15. Stress Cloud Map of Elastic Analysis Results.

4. Discussion

4.1. Mechanical Properties After Reinforcement

Post-reinforcement load tests revealed that the secondary cracking loads for A1, A2, and A3 were 15.00 kN, 18.00 kN, and 11.91 kN, respectively. Prior to cracking, the strain of the concrete upper flange (under compression) and lower flange (under tension) increased linearly with the load, with the CFRP plate effectively bearing the tensile force. The mid-span deflection of the reinforced beam was significantly reduced compared to pre-reinforcement levels; for instance, under a 50 kN load, the mid-span deflection of A1 was 5.47 mm, a 57.3% decrease from the pre-reinforcement value of 12.81 mm.

https://doi.org/10.3390/buildings16112065

4.2. Numerical Simulation and Verification of Theoretical Formulas

4.2.1. Numerical Simulation and Verification Analysis of Experimental Results

During the prestressing tensioning and reinforcement loading stages, experimental and simulation results were compared for the strain of concrete, steel reinforcement, and CFRP plates, as well as the beam deflection. The results demonstrated high consistency among the key mechanical parameters.

Tensioning stage: Strain changes linearly in segments with the tension force, exhibiting a distinct strain inflection point at crack closure. The correlation coefficient between nonlinear analysis and experimental data ranges from 0.95 to 0.99, with a maximum deviation of <5%, accurately reflecting the stress distribution under compression in concrete and CFRP plates. The comparison between simulated and experimental results of monitoring points at each section of concrete A1, A2 and A3 is shown in Figures 16–18.

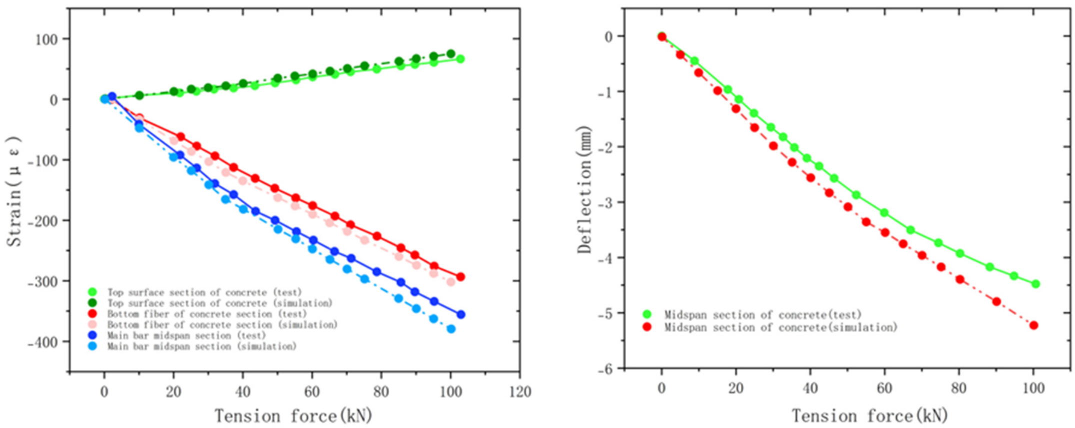

(**a**) Strain Comparison (**b**) Comparison of mid-span deflection

Figure 16. Comparison of Simulation Results and Test Results of Monitoring Points at Each Section of A1 Concrete.

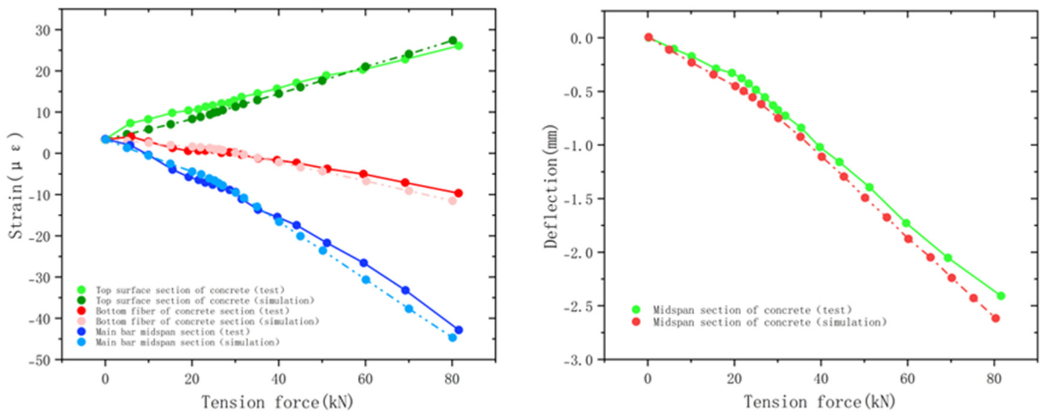

(**a**) Strain Comparison (**b**) Comparison of mid-span deflection

Figure 17. Comparison of Simulation Results and Test Results of Monitoring Points at Each Section of A2 Concrete.

During the loading phase, the simulated tensile strain at the concrete bottom edge and mid-span deflection matched experimental results, with a secondary cracking load deviation below 1 kN. The crack strain distribution in the web was consistent, demonstrating the model's effective crack capture capability. The simulated and experimental results of monitoring points at each section of A1, A2 and A3 concrete are shown in Figures 19–21.

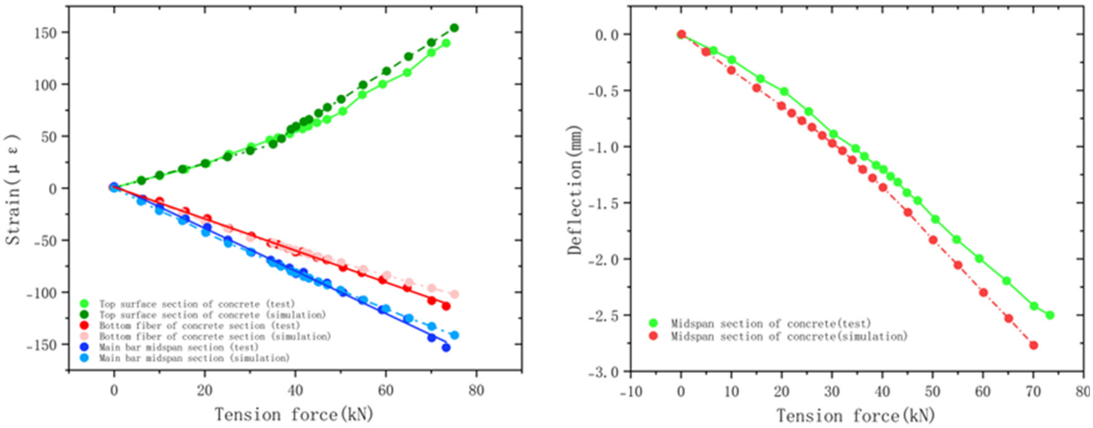

(**a**) Strain Comparison (**b**) Comparison of mid-span deflection

Figure 18. Comparison of Simulation Results and Test Results of Monitoring Points at Each Section of A3 Concrete.

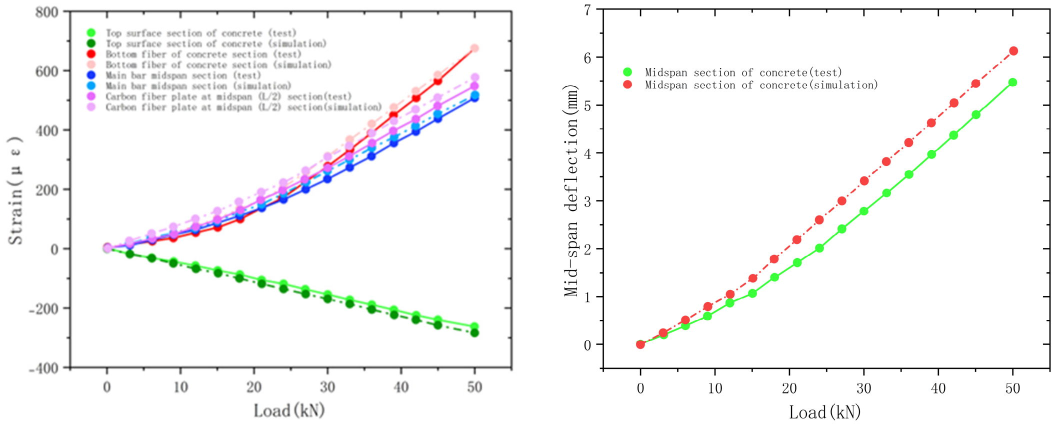

(**a**) Strain Comparison (**b**) Comparison of mid-span deflection

Figure 19. Comparison of Simulation Results and Test Results of Monitoring Points at Each Section of A1 Concrete.

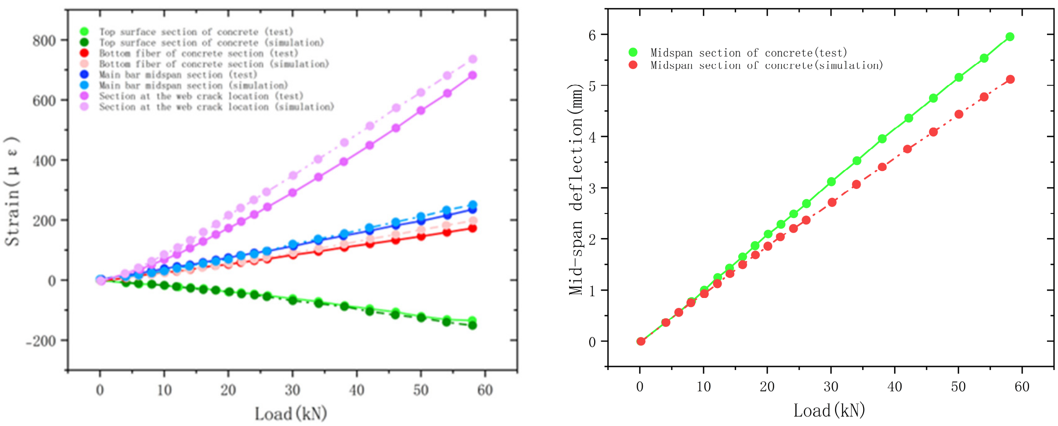

(**a**) Strain Comparison (**b**) Comparison of mid-span deflection

Figure 20. Comparison of Simulation Results and Test Results of Monitoring Points at Each Section of A2 Concrete.

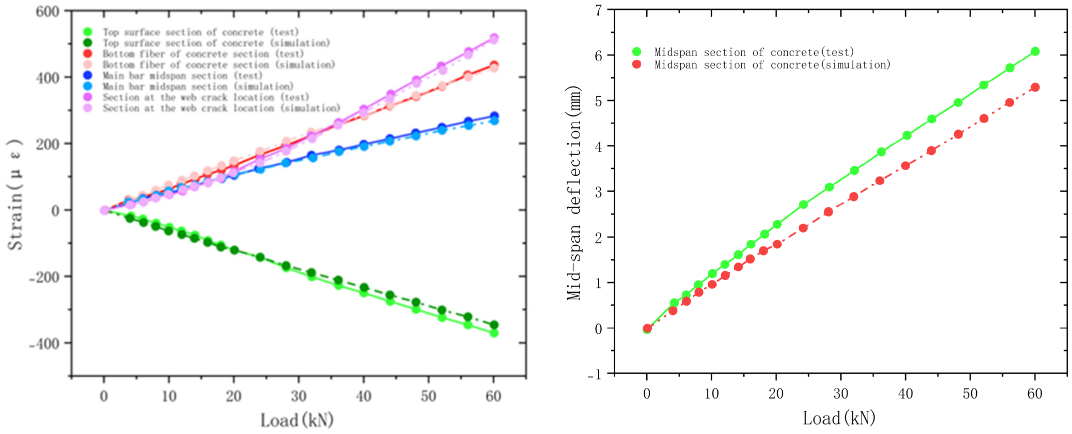

(**a**) Strain Comparison (**b**) Comparison of mid-span deflection

Figure 21. Comparison of Simulation Results and Test Results of Monitoring Points at Each Section of A3 Concrete.

- Tensioning stage of CFRP plate

Numerical simulations and experimental verification demonstrate that during the tensioning phase of the CFRP plate, the correlation coefficients between the nonlinear strain analysis results at the upper and lower edges of the concrete span, the center of the reinforcement, and the 1/2 L position of the CFRP plate and the experimentally measured values all range from 0.95 to 0.99, indicating high consistency between the results.

- Loading of T-beam after CFRP plate reinforcement

Numerical simulations and experimental verification demonstrate that after loading the T-beam reinforced with CFRP plates, the correlation coefficients between nonlinear strain analyses at the upper and lower edges of the concrete span, the reinforcement center, and crack locations in the web plate and experimental values all range from 0.93 to 0.99, indicating high consistency between the nonlinear results and experimental findings.

4.2.2. Deflection Error Analysis

Compared with strain-related indicators, the deflection prediction exhibited relatively larger deviations between numerical simulations and experimental measurements. During the CFRP tensioning stage, the relative errors of mid-span deflection under the maximum tension force were 16.52%, 8.71%, and 10.80% for specimens A1, A2, and A3, respectively (Table 9). During the post-strengthening loading stage, the relative errors of mid-span deflection under a 30 kN load were 22.66%, 12.50%, and 16.71% for A1, A2, and A3, respectively (Table 10). These errors were higher than those of CFRP strain prediction, which were generally within 3.97–11.47%, indicating that the numerical model reproduced the strain response more accurately than the global deformation response.

The relatively large deflection deviations can be attributed to several factors. First, the support and loading boundary conditions in the finite element model were idealized, whereas the actual test setup inevitably involved local contact deformation and slight support settlement. Second, anchorage slip and local deformation at the CFRP anchorage zone may have reduced the effective prestress transfer efficiency, which directly affected the measured camber and deflection. Third, the pre-cracking process introduced residual deformation and distributed microcracks in the concrete beam, while the numerical model mainly represented dominant cracks through the equivalent crack-width and element-deletion approach. This simplification may underestimate local stiffness degradation caused by microcrack accumulation. Fourth, concrete heterogeneity and bond-slip effects between reinforcement and concrete were not fully represented in the numerical model.

Table 9. Comparison of Tension Stage Test Results with Finite Element Simulation Results (Key Indicators).

Sample Number	Evaluating Indicator	Experimental Measured Value	Finite Element Simulation Values	Fractional Error (%)	Correlation R^2
A1	Crack closure prestress (kN)	35.70	37.55	5.18	0.98
	Strain of the CFRP plate under maximum tensile force (με)	3296.59	3529.15	7.05	0.99
	Mid-span deflection under maximum tension force (mm)	−4.48	−5.22	16.52	0.97
A2	Crack closure prestress (kN)	23.10	25.12	8.74	0.99
	Strain of the CFRP plate under maximum tensile force (με)	2675.17	2755.00	2.98	0.99
	Mid-span deflection under maximum tension force (mm)	−2.41	−2.62	8.71	0.98
A3	Crack closure prestress (kN)	34.60	36.85	6.50	0.98
	Strain of the CFRP plate under maximum tensile force (με)	5484.18	5689.00	3.73	0.99
	Mid-span deflection under maximum tension force (mm)	−2.50	−2.77	10.80	0.97

Note: Relative error = ∣simulated value-measured value∣/measured value × 100%.

Table 10. Comparison of Test Results and Finite Element Simulation Results during Post-Strengthening Loading Stage (Key Indicators).

Sample Number	Evaluating Indicator	Experimental Measured Value	Finite Element Simulation Values	Fractional Error (%)	Correlation R^2
A1	Secondary cracking load (kN)	15.00	13.84	7.73	0.99
	Mid-span deflection under a 30 kN load (mm)	2.78	3.41	22.66	0.93
	Strain (με) of CFRP plate under a 30 kN load	275.43	307.02	11.47	0.98
A2	Secondary cracking load (kN)	18.00	18.09	0.50	0.99
	Mid-span deflection under a 30 kN load (mm)	3.12	2.73	12.50	0.95
	Strain (με) of CFRP plate under a 30 kN load	113.40	117.90	3.97	0.99
A3	Secondary cracking load (kN)	11.91	14.31	20.15	0.94
	Mid-span deflection under a 30 kN load (mm)	3.47	2.89	16.71	0.93
	Strain (με) of CFRP plate under a 30 kN load	151.47	157.56	4.02	0.98

Although the deflection errors were relatively larger, the correlation coefficients for deflection response remained within 0.93–0.98, and the prediction errors of the critical crack-closure prestress and secondary cracking load remained within an acceptable engineering range. Therefore, the finite element model can still provide reliable support for evaluating the overall prestress-induced stiffness recovery and crack-closure behavior of externally prestressed CFRP-strengthened pre-cracked RC T-beams.

It should be noted that certain individual data points exhibited relatively large deviations. For specimen A3, the secondary cracking load exhibited a prediction error of 20.15%, which may be attributed to its higher reinforcement ratio (3.61%) and the associated confinement effect that delayed crack reopening beyond the model's prediction. For specimen A1, the mid-span deflection under 30 kN load showed an error of 22.66%, potentially resulting from the more severe pre-cracking damage in the low-reinforcement beam and the consequent larger residual deformation that was not fully captured by the equivalent crack-width simplification.

4.2.3. Verification and Analysis of Theoretical Formula Results

Based on the theoretical model, measure the width, length, and location of the beam cracks, then substitute the data into the formula to calculate the prestress required for crack closure. To verify the accuracy of this prestress, apply incremental loads to determine the load required for secondary cracking. The comparison of theoretical formula, finite element simulation and experimental measurement results is shown in Table 11.

Table 11. Triple comparison of theoretical formula, finite element simulation, and experimental measurement results.

Sample Number	Evaluating Indicator	Theoretical Calculated Value (kN) (k = 0.95)	Finite Element Simulation Values (kN)	Experimental Measured Value (kN)	Relative Error Between Theory and Experiment (%)	Relative Error Between Simulation and Experimental Results (%)
A1	Crack closure prestress	36.46	37.55	35.70	2.13	5.18
	Secondary cracking load	13.44	13.84	15.00	10.40	7.73
A2	Crack closure prestress	24.01	25.12	23.10	3.94	8.74
	Secondary cracking load	17.28	18.09	18.00	4.00	0.50
A3	Crack closure prestress	35.43	36.85	34.60	2.40	6.50
	Secondary cracking load	13.76	14.31	11.91	15.53	20.15

The validation results demonstrate the high accuracy of the theoretical calculation formula: the calculation error for crack closure prestress ranges from 2.99% to 4.62%, meeting the engineering error threshold ($\leq$5%). The numerical simulation accurately reproduces the crack closure process, with a closure prestress deviation of 2.08–3.79%, confirming its applicability under geometric nonlinearity. The calculation error for secondary cracking load is 2.98–4.69%, while the numerical simulation shows a critical load deviation of 4.17–13.44% and a data dispersion of 5.7%, indicating the model's high reliability in determining the critical point for secondary failure loads.

4.3. Stiffness Recovery Analysis

This study measured the stiffness of an external prestressed reinforced concrete beam, calculated the theoretical cracking stiffness according to the Code for Design of Concrete

Structures (GB 50010-2010), and converted it into the unit displacement load at the mid-span section of the T-beam to evaluate the reinforcement effectiveness. The measured stiffness data obtained using strain gauges and displacement sensors were compared, with the results presented in tables and charts (Table 12).

Table 12. Stiffness Results Comparison.

Sample Number	Stiffness Before Cracking (N/mm)	Stiffness After Cracking (N/mm)	Stiffness Before Reinforcement (N/mm)	Stiffness After Reinforcement (N/mm)	Stiffness Recovery Rate (%)	Stiffness After Reinforcement/ Stiffness After Cracking (%)
A1	20.06	10.26	7.61	11.89	156.2	115.9
A2	25.10	13.33	8.36	9.81	117.3	73.6
A3	31.27	15.09	8.63	9.02	104.5	59.8

Note: All stiffness values are measured at the mid-span section; Stiffness recovery rate = Post-reinforcement stiffness/Pre-reinforcement stiffness × 100%.

Experimental results indicate that prestressed reinforced concrete beams reinforced externally struggle to restore their stiffness to the undamaged state, primarily due to irreversible internal damage and constraints imposed by the anchoring system, force transfer paths, and deformation coordination. Stiffness tests demonstrate a strong correlation between measured stiffness and theoretical cracking stiffness (R^2 = 0.987), with measured values consistently stabilizing at approximately 1.3 times the theoretical value; thus, post-reinforcement stiffness should be corrected based on cracking stiffness. Among the three beams tested, Beam A1 exhibited a stiffness of 11.89.

The prestress level exhibits a nonlinear relationship with stiffness recovery, providing a basis for optimized design. Post-reinforcement stiffness improves significantly but does not fully recover, with A1 demonstrating the optimal effect due to proper prestress application. Stiffness attenuation stems from internal concrete damage and prestress transfer losses.

Discussion on the High Stiffness Recovery Ratio of Specimen A1

Among the three specimens, A1 exhibited the highest stiffness recovery ratio (156.2%). This phenomenon is mainly related to its relatively low reinforcement ratio and severe stiffness degradation before strengthening. Due to the lower longitudinal reinforcement ratio of A1, the beam experienced more pronounced crack-induced stiffness reduction during the pre-cracking stage. Consequently, after prestressed CFRP strengthening and crack closure, the relative improvement in structural stiffness became significantly larger than those of A2 and A3.

In addition, the externally applied prestress generated a more obvious reverse camber effect and compressive stress redistribution in A1, which effectively reduced tensile stress concentration around the cracks and improved the overall flexural stiffness of the beam.

It should also be noted that the stiffness recovery ratio is defined as the ratio between post-strengthening stiffness and pre-strengthening stiffness. Therefore, a relatively low initial stiffness before strengthening may naturally lead to a larger recovery ratio after reinforcement.

Furthermore, the observed stiffness recovery trend is consistent with the finite element simulation results and existing studies on prestressed CFRP-strengthened RC beams, indicating that the measured results possess acceptable rationality and engineering reliability.

4.4. Fracture Closure Prestress Engineering Correction Factor

To address the discrepancy between theory and k practice, an engineering correction factor was introduced to optimize the crack closure prestress calculation formula. This factor compensates for non-ideal factors such as prestress loss, anchoring efficiency, and material variability, enabling the theoretical model to be directly applied to external prestressing reinforcement projects of reinforced concrete beams.

4.4.1. Definitions and Physical Meaning

The engineering correction coefficient k is the ratio between the designed prestress P for actual engineering design and the theoretical crack-closing prestress P theory. The formula $P_{design} = P_{theory} \times k$ is used to compensate for non-ideal factors in actual engineering. k ensures complete crack closure while avoiding excessive reinforcement.

A value of k less than 1 indicates that the actual required prestress is lower than the theoretical value. This is because the ideal model does not account for the beneficial effects of prestress transfer gain and anchorage residual stress. The engineering correction factor k is the ratio of the prestress P_{design} used in practical engineering design to the theoretical crack-closing prestress P_{theory}. The formula $P_{design} = P_{theory} \times k$ is adopted to account for non-ideal factors in real engineering applications. The coefficient k ensures full crack closure while avoiding excessive strengthening.

Its value being less than 1 indicates that the actual required prestress is lower than the theoretical value, since the ideal model neglects the beneficial effects of prestress transfer enhancement and residual anchorage stress.

4.4.2. Core Deviation Sources and Quantification Basis

Based on experimental data and the Highway Bridge Reinforcement Design Code (JTG/T 522-2019), three core factors contributing to discrepancies between theoretical calculations and actual engineering conditions were identified and quantitatively defined.

Prestress loss: The prestress loss during tensioning is caused by the elastic shrinkage of CFRP plates, anchor slip, and elastic compression of concrete. The average prestress loss rate for the three test beams was 2.63%.

Anchoring efficiency: The actual anchoring reliability of clip-type anchors. The specification specifies that the minimum efficiency coefficient for external prestressed anchors shall be 0.95.

Material variability: The performance fluctuations of C40 concrete compressive strength and CFRP plate elastic modulus show a laboratory material coefficient of variation $\leq$ 5%, whereas the coefficient for materials procured in bulk for construction projects is approximately 8%.

4.4.3. Derivation of the Engineering Correction Factor

To improve the engineering applicability of the theoretical prestress model, the engineering correction factor k was calibrated through a weighted fitting procedure combining experimental deviation coefficients and practical engineering influence factors.

The calibration process consisted of four steps:

- Experimental deviation evaluation. For each specimen, the ratio between the experimentally measured crack-closure prestress and the theoretically calculated prestress was determined. The average deviation coefficient obtained from the three specimens was then calculated.
- Engineering influence evaluation. Based on JTG/T 522-2019 specifications and engineering experience, three major non-ideal factors were considered: prestress loss caused by anchorage slip, elastic shortening, and CFRP relaxation; anchorage efficiency of externally prestressed CFRP systems; material variability of concrete and CFRP plates.

An engineering influence coefficient was subsequently established according to the combined influence of these factors.

- Weighted fitting. The final correction coefficient was obtained through weighted fitting:

$$k = 0.7k_{exp} + 0.3k_{eng} \tag{37}$$

where k_{exp} = experimentally derived deviation coefficient and k_{eng} = engineering influence coefficient.

$$k_{exp} = \frac{1}{n}\sum_{i=1}^{n}\frac{P_{measured,i}}{P_{theory,i}} \tag{38}$$

$$k_{eng} = \eta_{anchor} \cdot \eta_{loss} \cdot \eta_{material} \tag{39}$$

where η_{anchor} = anchorage efficiency coefficient (0.95), η_{loss} = prestress loss coefficient (0.97), and $\eta_{material}$ = material variation coefficient (0.92–1.0).

The weighting factors were selected considering that experimental measurements should dominate the calibration process, while engineering influence factors serve as supplementary corrections for practical applications.

- Generalization to different geometries and loading conditions. For generalization to different member geometries (span lengths, section dimensions) and loading conditions (concentrated loads, uniformly distributed loads), the following adjustment procedure is recommended:

1. Determine the base correction coefficient k_{base} = 0.95 for standard T-beams with spans of 6–8 m under four-point bending.
2. Apply the span adjustment factor: for spans L differing from 6.8 m, $k_{span} = k_{base} \times \left(\frac{6.8}{L}\right)^{0.15}$, where the exponent 0.15 accounts for the mild dependence of prestress transfer efficiency on span-to-depth ratio.
3. Apply the section adjustment factor: for flange widths b_f between 400 and 800 mm, no adjustment is needed; for rectangular sections ($b_f = b_w$), reduce k by 0.01–0.02 due to reduced confinement effects.
4. For distributed loading conditions, increase k by 0.01 due to more uniform stress distribution compared to concentrated loads.

The calibrated correction coefficient ranged from 0.92 to 0.97, with 0.95 recommended as the conventional engineering value.

4.4.4. Verification of the Revised Formula

Taking Test Beam A1 as the verification object, substituting $k = 0.95$ into the modified Formula (31) to verify the calculation accuracy:

Theoretical crack-closing prestress: $P_{theory} = 36.46$ kN;

Engineering design prestress: $P_{design} = P_{theory} \times k = 36.46 \times 0.95 = 34.64$ kN;

Measured prestress from test: $P_{measured} = 35.70$ kN;

Relative error: $|34.64 - 35.70|/35.70 \times 100\% = 2.96\%$

Verification results show that the calculation error of the modified formula is $\leq$3.0%, which is much lower than the 5% error threshold permitted in engineering practice, confirming the accuracy and reliability of the modified formula.

4.4.5. Sensitivity Analysis of Correction Factor k

To evaluate the sensitivity of the proposed prestress model to the correction factor k, different k values ranging from 0.92 to 0.97 were analyzed. The results indicated that k = 0.95 provided the minimum average prediction error for crack-closure prestress among the investigated specimens.

When k was smaller than 0.94, the calculated prestress tended to underestimate the required crack-closure prestress. Conversely, when k exceeded 0.96, the calculated prestress became relatively conservative and resulted in larger prediction deviations. Therefore,

k = 0.95 is considered an appropriate balance between theoretical accuracy and engineering safety.

This sensitivity analysis further demonstrates the rationality and stability of the proposed correction coefficient.

4.4.6. Project Applicability

By fine-tuning the values according to the varying k degrees of impact from non-ideal factors across different engineering scenarios, the precision of reinforcement design can be further enhanced. The recommended values for each scenario are presented in Table 13.

Table 13. Recommended value for k.

Engineering Scenario Classification	**Recommended k value Range**	**Core Adjustment Basis**	**Engineering Scenario Classification**
Laboratory precision testing scenario	0.96~0.97	Pre-stress loss <1%; anchorage efficiency ≈1.0; material dispersion ≤5%	Scientific research testing, model calibration, and precise performance verification
Conventional highway bridge engineering (new construction/medium-scale renovation)	0.94~0.95	Prestress loss ≈ 2.63%; anchorage efficiency = 0.95; material variability ≈ 8%	Reinforcement of urban arterial roads and beam bridges with a service life of ≤15 years
Bridge engineering in harsh environments (coastal/high humidity/corrosive conditions)	0.93~0.94	Pre-stress loss ≈ 3.5%; anchorage efficiency = 0.93–0.94; material variability ≈ 10%	Reinforcement of coastal/erosion-prone beam bridges with a service life of 15–25 years
An aging bridge with severe cracks and damage	0.92~0.93	Pre-stress loss ≈ 4%; anchorage efficiency = 0.92–0.93; material variability ≈ 12%	Reinforcement of beam bridges with a service life > 25 years and crack width > 0.3 mm
Special Heavy-Duty Bridge Engineering	0.95~0.96	Pre-stress loss ≈ 2%; anchorage efficiency = 0.97–0.98; material dispersion ≤ 6%	Reinforcement of heavy-load bridges such as expressways and port terminals

Although the present study demonstrates satisfactory agreement among experimental results, theoretical calculations, and finite element simulations, several limitations should be acknowledged.

First, the experimental program included only three specimens with different reinforcement ratios. While the combined experimental–numerical–theoretical validation improves the reliability of the conclusions, the limited sample size restricts the statistical generalization of the proposed method. Future studies should incorporate larger specimen populations and probabilistic analyses to further evaluate parameter sensitivity and engineering reliability.

Second, the crack morphology considered in this study was simplified using an equivalent crack-width representation. Actual reinforced concrete structures often exhibit more complex three-dimensional crack networks and damage interactions under long-term service conditions.

Third, the proposed prestress calculation model is established under the plane-section assumption and engineering simplifications. Although the assumption remained reasonably valid before secondary cracking according to the measured strain distributions, severe nonlinear cracking conditions may reduce its applicability.

Finally, the finite element crack simulation employed an element-deletion-based equivalent crack method. The adopted approach is suitable for engineering-level crack-closure prestress evaluation; however, it does not explicitly simulate progressive crack propagation, fracture energy dissipation, or adaptive crack evolution. Future work may incorporate cohesive zone models or fracture-mechanics-based approaches to improve simulation fidelity.

4.4.7. Comparison with Existing Design Specifications

Existing reinforcement design specifications, such as GB50367-2013 and JTG/T 5431-2025, primarily adopt simplified assumptions based on crack-free or idealized single-crack conditions. In contrast, the present study incorporates explicit crack characteristics, prestress transfer effects, and engineering correction factors into the prestress evaluation framework.

Compared with existing specification-based approaches, the proposed method demonstrates improved adaptability for pre-cracked reinforced concrete members with complex crack distributions. The proposed framework also provides enhanced prediction accuracy for crack-closure prestress and secondary cracking loads while maintaining acceptable engineering simplicity. The comparison results are shown in Table 14.

Table 14. Quantitative comparison between existing design approaches and the proposed method.

Method	Crack Consideration	Average Prediction Error of Crack-Closure Prestress	Secondary Cracking Load Prediction Error	Ability to Consider Crack Morphology	Engineering Applicability
GB50367-2013	Crack-free simplified assumption	Typically >15% under multi-crack conditions	>20%	No	High
JTG/T 5431-2025	Simplified single-crack assumption	Approximately 10–15%	10–18%	Limited	High
Present study	Explicit crack width and crack morphology	2.99–4.62%	2.98–4.69%	Yes	Medium–High

The comparison demonstrates that the proposed method reduces the prediction error of crack closure prestress from over >15% (GB50367-2013) and 10–15% (JTG/T 5431-2025) to 2.99–4.62%, while maintaining computational simplicity through a closed-form formula and calibration correction coefficients. Existing specification-based methods are suitable for conventional engineering design under simplified crack conditions; however, their prediction accuracy declines when dealing with complex crack distributions. By explicitly incorporating crack width, crack morphology, and engineering correction coefficients, this method significantly improves the prediction accuracy of crack closure prestress and secondary crack loads while maintaining acceptable practical applicability.

5. Conclusions

This study focuses on prestressed CFRP plate-reinforced concrete beam bridges to investigate the correlation between crack information and external prestress. The main conclusions are as follows:

- Three prestressed T-beams with different reinforcement ratios were subjected to reinforcement tests, yielding critical data including strain measurements of concrete, steel reinforcement, and CFRP plates during tensioning and loading phases, mid-span deflection values, as well as the critical prestress required for crack closure and secondary cracking loads. The study elucidated the relationship between reinforcement ratio and crack closure behavior as well as stiffness recovery: higher reinforcement ratios correspond to greater initial stiffness, higher required prestress for crack closure, and enhanced deformation resistance post-reinforcement.

- Based on the plane section assumption, deformation compatibility and moment equilibrium principles, a mathematical model of external prestress, crack width and crack length was established, and the calculation formula for external prestress was derived: $N = \frac{f \times y_s}{y_c} = \frac{E_s w n \pi d^2 y_s}{4 L y_c}$. Aiming at the deviation between theoretical and actual results, three major influencing factors were identified: prestress loss, anchorage efficiency and material discreteness. A correction coefficient k (conventionally taken as 0.95, ranging from 0.92 to 0.97) was introduced by the weighted fitting method. After correction, the errors of crack-closing prestress and secondary cracking load are 2.99%~4.62% and 2.98%~4.69%, respectively, both lower than the allowable error of 5%. Nevertheless, the proposed method is currently more suitable for engineering-oriented prestress evaluation of pre-cracked RC beams, and further studies involving larger datasets, complex crack networks, and long-term durability effects are still required.
- A three-dimensional finite element model incorporating material constitutive laws and crack morphology was developed using Midas FEA NX 2022. The model employs plastic damage models for concrete, double-bilinear elastic–plastic models for steel reinforcement, and linear elastic constitutive laws for CFRP plates, combined with solid element mesh reduction and the equivalent width method to accurately simulate cracks. The model results exhibit excellent agreement with both experimental data and theoretical predictions, with correlation coefficients ranging from 0.93 to 0.99, demonstrating the accuracy and reliability of both the theoretical and numerical models.

Author Contributions: Conceptualization, J.H. and S.C.; methodology, J.H. and P.K.; software, J.H.; validation, J.H., S.C. and Z.M.; formal analysis, J.H.; investigation, J.H. and R.W.; resources, S.C.; data curation, J.H.; writing—original draft preparation, J.H.; writing—review and editing, S.C. and P.K.; visualization, J.H.; supervision, S.C.; project administration, S.C.; funding acquisition, S.C. All authors have read and agreed to the published version of the manuscript.

Funding: This research received no external funding.

Data Availability Statement: The data that support the findings of this study are available from the corresponding author upon reasonable request.

Acknowledgments: The authors would like to acknowledge the laboratory support provided for this study.

Conflicts of Interest: Author Peng Kang was employed by Yunnan Institute of Building Research Co., Ltd. The remaining authors declare that this study was conducted in the absence of any commercial or financial relationships that could be construed as a potential conflict of interest. The affiliation of Author Peng Kang with Yunnan Institute of Building Research Co., Ltd. did not influence the design, execution, or reporting of this research in any manner.

Abbreviations

The following abbreviations are used in this manuscript:

CFRP	Carbon Fiber-Reinforced Polymer
RC	Reinforced Concrete
HRB	Hot-rolled Ribbed Bar
MTS	Material Testing System
GB	Guobiao (Chinese National Standard)
JTG	Jiaotong Gonglu (China Ministry of Transport Standard)
R^2	Coefficient of determination

References

1. Chen, L.; Qiang, X.; Jiang, X.; Dong, H.; Chen, W. Study on Prestressed Concrete Beams Strengthened with External Unbonded CFRP Tendons. *Materials* **2024**, *17*, 4622. [CrossRef]
2. Wang, H.; Li, C.; Song, S.; Wang, Y.; Meng, Q.; Li, F. Flexural Performance of Cracked Reinforced Concrete Beams Strengthened with Prestressed CFRP Sheets under Repeated Loads. *Buildings* **2023**, *13*, 2115. [CrossRef]
3. Rodrigues, A.; Paulo, J.; Rosa, D. Nonlinear Numerical Analysis of Prestressed Concrete Beams and Slabs. *Eng. Struct.* **2020**, *223*, 111187. [CrossRef]
4. Li, B.; Zeng, L.; Guo, X.; Wang, Y.; Deng, Z. Flexural Behavior of Full-Scale Damaged Hollow RC Beams Strengthened with Prestressed SCFRP Plate under Four-Point Bending. *Polymers* **2022**, *14*, 2939. [CrossRef]
5. *China Transportation Yearbook 2022*; China Transportation Yearbook Press, Ministry of Transport of the People's Republic of China: Beijing, China, 2022.
6. Wang, H.-T.; Bian, Z.-N.; Xu, G.-W.; Chen, M.-S.; Xiong, H.; Liu, S.-S. Flexural Strengthening of Large-Scale RC Beams with Nonprestressed and Prestressed CFRP Using Different Anchorages. *Polymers* **2022**, *14*, 5498. [CrossRef] [PubMed]
7. *GB 50367-2013*; Design Code for Reinforcement of Concrete Structures. Ministry of Housing and Urban-Rural Development of the People's Republic of China: Beijing, China, 2013.
8. *JTG/T 5431-2025*; Design Code for Highway Bridge Reinforcement. Ministry of Transport of the People's Republic of China: Beijing, China, 2025.
9. Haroon, M.; Moon, J.S.; Kim, C. Performance of Reinforced Concrete Beams Strengthened with Carbon Fiber Reinforced Polymer Strips. *Materials* **2021**, *14*, 5866. [CrossRef] [PubMed]
10. Lutz, L.A. Analysis of Cracked Concrete Structures. *J. Struct. Div.* **1983**, *109*, 165–181.
11. Jalali, S.; Saouma, V.E. Assessment and Repair of Cracked Concrete Bridges: Part I—Cracking and Deflection Survey. *J. Struct. Eng.* **1990**, *116*, 3059–3077.
12. Panagiotakos, T.B.; Fardis, M.N. Effect of Cracking on Bond of Deformed Bars in Tension. *ACI Struct. J.* **1994**, *91*, 271–279.
13. Li, Z.; Soroushian, P. Stress Increment in External Tendons of Prestressed Concrete Beams. *J. Struct. Eng.* **1996**, *122*, 1463–1470.
14. Liu, Y.Q.; Yeoh, J.K.W. Automated crack pattern recognition from images for condition assessment of concrete structures. *Autom. Constr.* **2021**, *128*, 103765. [CrossRef]
15. Jiang, Q.; Wang, H.Q.; Chong, X.; Feng, Y.L.; Ye, X.G. Flexural behavior of high-strength, steel-reinforced, and prestressed concrete beams. *Front. Struct. Civ. Eng.* **2021**, *15*, 227–243. [CrossRef]
16. Zhang, S.Q.; Du, S.Z.; Ang, Y.; Lu, Z.B. Study on performance of prestressed concrete hollow slab beams reinforced by grouting with ultra-high performance concrete. *Case Stud. Constr. Mater.* **2021**, *15*, e00583. [CrossRef]
17. Shayanfar, J.; Barros, J.A.; Rezazadeh, M.; Kafshgarkolaei, H.J. Enhancing the performance of heat-damaged rectangular RC columns using prestressed FRP confinement. *Constr. Build. Mater.* **2025**, *501*, 144346. [CrossRef]
18. Ranjbar, F.; Asgari, A.; Bagheri, M.; Bengar, H.A. Insights into the mechanisms and seismic performance of reinforced concrete buildings on a pile foundation in liquefiable deposits. *Structures* **2026**, *87*, 111557. [CrossRef]
19. Xu, F.; Li, D.; Zhao, J.; Huang, J. Experimental Study on Prestressed Carbon Fiber Plate Reinforcement of Reinforced Concrete Beams. *Build. Struct.* **2010**, *40*, 372–375. (In Chinese)
20. *JTG 3362-2018*; Design Code for Highway Reinforced Concrete and Prestressed Concrete Bridges and Culverts. Ministry of Transport of the People's Republic of China: Beijing, China, 2018.
21. Schiavoni, M.; Giordano, E.; Roscini, F.; Clementi, F. Advanced numerical insights for an effective seismic assessment of historical masonry aggregates. *Eng. Struct.* **2023**, *285*, 115997. [CrossRef]
22. *JTG/T 522-2019*; Design Code for Reinforcement of Highway Bridges. Ministry of Transport of the People's Republic of China: Beijing, China, 2019.
23. Fang, Z. *Finite Element Analysis Method for Bridge Structures*; China Communications Press: Beijing, China, 2012.
24. Kuchma, D.A.; Frosch, R.J. Finite-Element Analysis of Prestressed Concrete Beams with Externally Bonded FRP Tendons. *J. Compos. Constr.* **2002**, *6*, 187–195.
25. Buyle-Bodin, F.; David, E.; Ragneau, E. Finite Element Modelling of Flexural Behaviour of Externally Bonded CFRP Reinforced Concrete Structures. *Eng. Struct.* **2002**, *24*, 1423–1429. [CrossRef]
26. *GB 50010-2010*; Code for Design of Concrete Structures. Ministry of Housing and Urban-Rural Development of the People's Republic of China: Beijing, China, 2010.
27. Cramer, J.; Javidmehr, S.; Empelmann, M. Simulation of Crack Propagation in Reinforced Concrete Elements. *Appl. Sci.* **2021**, *11*, 785. [CrossRef]
28. Goszczyńska, B.; Trąmpczyński, W.; Tworzewska, J. Analysis of Crack Width Development in Reinforced Concrete Beams. *Materials* **2021**, *14*, 3043. [CrossRef]
29. Wang, W.W.; Dai, J.G.; Harries, K.A.; Bao, Q.H. Prestress Losses and Flexural Behavior of Reinforced Concrete Beams Strengthened with Posttensioned CFRP Sheets. *J. Compos. Constr.* **2012**, *16*, 207–216. [CrossRef]

30. Wang, W.; Dai, J.; Zhang, L. Study on the Experimental and Computational Methods for Assessing Prestress Loss in Post-Stressed Carbon Fiber Cloth-Reinforced Reinforced Concrete Beams. *China Civ. Eng. J.* **2012**, *45*, 88–94. (In Chinese)
31. Zhou, K.; Liu, Z.; Yue, L.; Zhao, W.; Liang, B.; Song, D. Numerical Analysis of the Mechanical Performance of Prestressed Carbon Fiber Fabric-Reinforced Secondary Reinforced Concrete Beams. *Earthq. Eng. Eng. Vib.* **2014**, *36*, 79–85. (In Chinese)
32. Shi, Y. Research on the Performance of CFRP-Reinforced Partial Prestressed Concrete Beams. Master's Thesis, Hebei University of Technology, Tianjin, China, 2017. (In Chinese)